

# Planck intermediate results. XXXVIII. *E*- and *B*-modes of dust polarization from the magnetized filamentary structure of the interstellar medium

Planck Collaboration: P. A. R. Ade<sup>81</sup>, N. Aghanim<sup>55</sup>, M. Arnaud<sup>69</sup>, M. Ashdown<sup>66,5</sup>, J. Aumont<sup>55</sup>, C. Baccigalupi<sup>80</sup>, A. J. Banday<sup>89,9</sup>, R. B. Barreiro<sup>61</sup>, N. Bartolo<sup>28,62</sup>, E. Battaner<sup>91,92</sup>, K. Benabed<sup>56,88</sup>, A. Benoit-Lévy<sup>22,56,88</sup>, J.-P. Bernard<sup>89,9</sup>, M. Bersanelli<sup>31,47</sup>, P. Bielewicz<sup>77,9,80</sup>, A. Bonaldi<sup>64</sup>, L. Bonavera<sup>61</sup>, J. R. Bond<sup>8</sup>, J. Borrill<sup>12,85</sup>, F. R. Bouchet<sup>56,83</sup>, F. Boulanger<sup>55</sup>, A. Bracco<sup>55</sup>, C. Burigana<sup>46,29,48</sup>, E. Calabrese<sup>87</sup>, J.-F. Cardoso<sup>70,1,56</sup>, A. Catalano<sup>71,68</sup>, A. Chaballu<sup>69,14,55</sup>, R.-R. Chary<sup>53</sup>, H. C. Chiang<sup>25,6</sup>, P. R. Christensen<sup>78,33</sup>, L. P. L. Colombo<sup>21,63</sup>, C. Combet<sup>71</sup>, B. P. Crill<sup>63,10</sup>, A. Curto<sup>5,61</sup>, F. Cuttaia<sup>46</sup>, L. Danese<sup>80</sup>, R. D. Davies<sup>64</sup>, R. J. Davis<sup>64</sup>, P. de Bernardis<sup>30</sup>, A. de Rosa<sup>46</sup>, G. de Zotti<sup>43,80</sup>, J. Delabrouille<sup>1</sup>, J.-M. Delouis<sup>56,88</sup>, C. Dickinson<sup>64</sup>, J. M. Diego<sup>61</sup>, H. Dole<sup>55,54</sup>, S. Donzelli<sup>47</sup>, O. Doré<sup>63,10</sup>, M. Douspis<sup>55</sup>, J. Dunkley<sup>87</sup>, X. Dupac<sup>35</sup>, G. Efstathiou<sup>57</sup>, F. Elsner<sup>22,56,88</sup>, T. A. Enßlin<sup>75</sup>, H. K. Eriksen<sup>58</sup>, E. Falgarone<sup>68</sup>, K. Ferrière<sup>89,9</sup>, F. Finelli<sup>46,48</sup>, O. Forni<sup>89,9</sup>, M. Frailis<sup>45</sup>, A. A. Fraisse<sup>25</sup>, E. Franceschi<sup>46</sup>, A. Frolov<sup>82</sup>, S. Galeotta<sup>45</sup>, S. Galli<sup>65</sup>, K. Ganga<sup>1</sup>, T. Ghosh<sup>55</sup>\*, M. Giard<sup>89,9</sup>, E. Gjerløw<sup>58</sup>, J. González-Nuevo<sup>18,61</sup>, K. M. Górski<sup>63,93</sup>, A. Gruppuso<sup>46</sup>, V. Guillet<sup>55</sup>, F. K. Hansen<sup>58</sup>, D. L. Harrison<sup>57,66</sup>, G. Helou<sup>10</sup>, C. Hernández-Monteagudo<sup>11,75</sup>, D. Herranz<sup>61</sup>, S. R. Hildebrandt<sup>63,10</sup>, E. Hivon<sup>56,88</sup>, A. Hornstrup<sup>15</sup>, W. Hovest<sup>75</sup>, Z. Huang<sup>8</sup>, K. M. Huffenberger<sup>23</sup>, G. Hurier<sup>55</sup>, T. R. Jaffe<sup>89,9</sup>, W. C. Jones<sup>25</sup>, M. Juvela<sup>24</sup>, E. Keihänen<sup>24</sup>, R. Keskitalo<sup>12</sup>, T. S. Kisner<sup>73</sup>, R. Kneissl<sup>34,7</sup>, J. Knoche<sup>75</sup>, M. Kunz<sup>16,55,3</sup>, H. Kurki-Suonio<sup>24,41</sup>, J.-M. Lamarre<sup>68</sup>, A. Lasenby<sup>5,66</sup>, M. Lattanzi<sup>29</sup>, C. R. Lawrence<sup>63</sup>, R. Leonardi<sup>35</sup>, J. León-Tavares<sup>59,38,2</sup>, F. Levrier<sup>68</sup>, M. Liguori<sup>28,62</sup>, P. B. Lilje<sup>58</sup>, M. Linden-Vørnle<sup>15</sup>, M. López-Cañiego<sup>35,61</sup>, P. M. Lubin<sup>26</sup>, J. F. Macías-Pérez<sup>71</sup>, B. Maffei<sup>64</sup>, D. Maino<sup>31,47</sup>, N. Mandolesi<sup>46,29</sup>, M. Maris<sup>45</sup>, P. G. Martin<sup>8</sup>, E. Martínez-González<sup>61</sup>, S. Masi<sup>30</sup>, S. Matarrese<sup>28,62,39</sup>, P. McGehee<sup>53</sup>, A. Melchiorri<sup>30,49</sup>, A. Mennella<sup>31,47</sup>, M. Migliaccio<sup>57,66</sup>, M.-A. Miville-Deschênes<sup>55,8</sup>, A. Moneti<sup>56</sup>, L. Montier<sup>89,9</sup>, G. Morgante<sup>46</sup>, D. Mortlock<sup>52</sup>, D. Munshi<sup>81</sup>, J. A. Murphy<sup>76</sup>, P. Naselsky<sup>78,33</sup>, F. Nati<sup>25</sup>, P. Natoli<sup>29,4,46</sup>, D. Novikov<sup>74</sup>, I. Novikov<sup>78,74</sup>, N. Oppermann<sup>8</sup>, C. A. Oxborrow<sup>15</sup>, L. Pagano<sup>30,49</sup>, F. Pajot<sup>55</sup>, D. Paoletti<sup>46,48</sup>, F. Pasian<sup>45</sup>, O. Perdereau<sup>67</sup>, V. Pettorino<sup>40</sup>, F. Piacentini<sup>30</sup>, M. Piat<sup>1</sup>, E. Pierpaoli<sup>21</sup>, S. Plaszczynski<sup>67</sup>, E. Pointecouteau<sup>89,9</sup>, G. Polenta<sup>4,44</sup>, N. Ponthieu<sup>55,51</sup>, G. W. Pratt<sup>69</sup>, S. Prunet<sup>56,88</sup>, J.-L. Puget<sup>55</sup>, J. P. Rachen<sup>19,75</sup>, W. T. Reach<sup>90</sup>, R. Rebolo<sup>60,13,17</sup>, M. Reinecke<sup>75</sup>, M. Remazeilles<sup>64,55,1</sup>, C. Renault<sup>71</sup>, A. Renzi<sup>32,50</sup>, I. Ristorcelli<sup>89,9</sup>, G. Rocha<sup>63,10</sup>, C. Rosset<sup>1</sup>, M. Rossetti<sup>31,47</sup>, G. Roudier<sup>1,68,63</sup>, J. A. Rubiño-Martín<sup>60,17</sup>, B. Rusholme<sup>53</sup>, M. Sandri<sup>46</sup>, D. Santos<sup>71</sup>, M. Savelainen<sup>24,41</sup>, G. Savini<sup>79</sup>, D. Scott<sup>20</sup>, P. Serra<sup>55</sup>, J. D. Soler<sup>55</sup>, V. Stolyarov<sup>5,66,86</sup>, R. Sudiwala<sup>81</sup>, R. Sunyaev<sup>75,84</sup>, A.-S. Suur-Uuski<sup>24,41</sup>, J.-F. Sygnet<sup>56</sup>, J. A. Tauber<sup>36</sup>, L. Terenzi<sup>37,46</sup>, L. Toffolatti<sup>18,61,46</sup>, M. Tomasi<sup>31,47</sup>, M. Tristram<sup>67</sup>, M. Tucci<sup>16</sup>, G. Umama<sup>42</sup>, L. Valenziano<sup>46</sup>, J. Valiviita<sup>24,41</sup>, B. Van Tent<sup>72</sup>, P. Vielva<sup>61</sup>, F. Villa<sup>46</sup>, L. A. Wade<sup>63</sup>, B. D. Wandelt<sup>56,88,27</sup>, I. K. Wehus<sup>63</sup>, D. Yvon<sup>14</sup>, A. Zacchei<sup>45</sup>, and A. Zonca<sup>26</sup>

(Affiliations can be found after the references)

Preprint online version: August 6, 2018

## ABSTRACT

The quest for a *B*-mode imprint from primordial gravity waves on the polarization of the cosmic microwave background (CMB) requires the characterization of foreground polarization from Galactic dust. We present a statistical study of the filamentary structure of the 353 GHz *Planck* Stokes maps at high Galactic latitude, relevant to the study of dust emission as a polarized foreground to the CMB. We filter the intensity and polarization maps to isolate filaments in the range of angular scales where the power asymmetry between *E*-modes and *B*-modes is observed. Using the Smoothed Hessian Major Axis Filament Finder (SMAFF), we identify 259 filaments at high Galactic latitude, with lengths larger or equal to  $2^\circ$  (corresponding to 3.5 pc in length for a typical distance of 100 pc). These filaments show a preferred orientation parallel to the magnetic field projected onto the plane of the sky, derived from their polarization angles. We present mean maps of the filaments in Stokes *I*, *Q*, *U*, *E*, and *B*, computed by stacking individual images rotated to align the orientations of the filaments. Combining the stacked images and the histogram of relative orientations, we estimate the mean polarization fraction of the filaments to be 11%. Furthermore, we show that the correlation between the filaments and the magnetic field orientations may account for the *E* and *B* asymmetry and the  $C_\ell^{TE}/C_\ell^{EE}$  ratio, reported in the power spectra analysis of the *Planck* 353 GHz polarization maps. Future models of the dust foreground for CMB polarization studies will need to take into account the observed correlation between the dust polarization and the structure of interstellar matter.

**Key words.** Polarization – ISM: general – Galaxy: ISM – submillimeter: ISM

\* Corresponding author: tuhin.ghosh@ias.u-psud.fr

## 1. Introduction

Recently, *Planck*<sup>1</sup> has reported an asymmetry in power between the dust *E*- and *B*-modes in its 353 GHz observations (Planck Collaboration Int. XXX 2014; Planck Collaboration X 2015). This power asymmetry has been observed outside masks covering 20 to 70% of the sky, excluding the Galactic plane. The ratio of the dust *B*- to *E*-mode power amplitudes is about a half over the multipole range  $40 < \ell < 600$  (Planck Collaboration Int. XXX 2014). The source of this power asymmetry in the dust polarization data is currently unknown. Models of the Galactic magnetic field (GMF) used in the Planck sky model (PSM, Delabrouille et al. 2013) and the FGPOL model (O’Dea et al. 2012) produce an equal amount of power in *E*- and *B*-modes outside the regions covered by the sky masks. These models, which were used to estimate the dust polarization foreground (BICEP2 Collaboration 2014; BICEP2/Keck Array and Planck Collaborations 2015), include an analytical model of the large-scale GMF ( $\mathbf{B}_{\text{GMF}}$ ) and a statistical description of the turbulent component of the magnetic field.

The *Planck* maps of thermal dust emission display filaments distributed over the whole sky (Planck Collaboration XI 2014). The filamentary structure of the diffuse interstellar matter is also a striking feature of dust observations at higher angular resolution, performed by *Herschel*, and of spectroscopic H $\alpha$  observations (e.g. Miville-Deschênes et al. 2010; André et al. 2014; Clark et al. 2014). The analysis of *Planck* dust polarization data in the diffuse interstellar medium (ISM), at low and intermediate Galactic latitudes, indicates that the structures of interstellar matter tend to be aligned with the plane of the sky (POS) projection of the magnetic field ( $\mathbf{B}_{\text{POS}}$ , Planck Collaboration Int. XXXII 2014). This preferential relative orientation is also observed in simulations of magneto-hydrodynamic (MHD) turbulence of the diffuse ISM (Hennebelle 2013; Soler et al. 2013). Such a coupling between the structure of interstellar matter and  $\mathbf{B}_{\text{POS}}$  is not included in the PSM or FGPOL models of the dust polarization sky (Delabrouille et al. 2013; O’Dea et al. 2012).

The goal of this paper is to test whether the correlation between the filamentary structures of the intensity map and  $\mathbf{B}_{\text{POS}}$  in the diffuse ISM accounts for the observed *E*-*B* asymmetry. Zaldarriaga (2001) describes the *E*- and *B*-modes decomposition of simple patterns of polarized emission, including filaments with a homogeneous polarization degree and orientation. The presence of *E*-modes is related to invariance by parity of the polarization pattern. There is *E*-only power if  $\mathbf{B}_{\text{POS}}$  is either parallel or perpendicular to the filaments. If  $\mathbf{B}_{\text{POS}}$  is oriented at  $+45^\circ$  or  $-45^\circ$  with respect to the filaments, there is *B*-only power.

In this paper, we filter the *Planck* intensity and polarization maps to isolate filaments in the range of angular scales where the *E*-*B* asymmetry is observed. We identify coherent elongated filaments within regions of low column density at high Galactic latitude using a filament-finding algorithm. We evaluate the mean polarization angle in each of these filaments and compare it to the mean orientation of each filament. In doing so, we extend the analysis presented in Planck Collaboration Int. XXXII (2014) to the relevant region of the sky for CMB polarization observations at high Galactic latitude. In order to achieve a high signal-to-

noise ratio and enhance the contrast with respect to the local background dust emission, we stack the Stokes *I*, *Q*, *U*, and also *E* and *B* maps, for the filaments we select in the *Planck* dust intensity map. We use the stacked images to quantify the power asymmetry in *E*- and *B*-modes associated with the filaments.

This paper is organized as follows. In Sect. 2, we introduce the *Planck* 353 GHz data used in this study. The filament-finding algorithm is presented in Sect. 3. Section 4 presents the study of relative orientation between the filaments,  $\mathbf{B}_{\text{POS}}$ , and the POS component of the large-scale GMF ( $\mathbf{B}_{\text{m,POS}}$ ) at high Galactic latitude. In Sect. 5, we present the stacking of both intensity and polarization maps and derive the mean polarization fraction of the filaments. In Sect. 6, we discuss the relation between the relative orientation of the filaments and  $\mathbf{B}_{\text{POS}}$  and the *E*-*B* asymmetry. Section 7 presents our results in the context of earlier studies and its relation to Galactic astrophysics. Finally, we present our conclusions in Sect. 8. This paper has four appendices. Appendix A details the Hessian analysis implemented to identify the filaments in the dust intensity map. The application of the filament-finding algorithm to a simulated Gaussian dust sky is detailed in Appendix B. In Appendix C, we study the impact of our selection of the filaments on the main results of the paper. The computation of all the angle uncertainties that we use in our analysis is presented in Appendix D.

## 2. Planck data

The *Planck* satellite has observed the sky polarization in seven frequency bands from 30 to 353 GHz (Planck Collaboration I 2015). In this paper, we only use the 2015 (“DX11d”) data from the High Frequency Instrument (HFI, Lamarre et al. 2010) at 353 GHz, since they are best suited to study the structure of dust polarization (Planck Collaboration Int. XIX 2015; Planck Collaboration Int. XX 2015; Planck Collaboration Int. XXI 2015; Planck Collaboration Int. XXII 2015). The data processing, map-making, and calibration of the HFI data are described in Planck Collaboration VII (2015) and Planck Collaboration VIII (2015). In our analysis, we ignore the dust and CO spectral mismatch leakage from intensity to polarization (Planck Collaboration VIII 2015). Planck Collaboration Int. XXX (2014) has shown that the amplitude of the dust spectral mismatch leakage at high latitude ( $f_{\text{sky}} = 0.5$ ) is small compared to the total polarization signal in *E* and *B* modes. No CO emission is detected at 353 GHz away from the Galactic plane and the brightest molecular clouds (Planck Collaboration XIII 2014) and so we do not consider it in our analysis.

To quantify the statistical noise and systematic effects on the results presented in this paper, we use the two HalfMission (HM), two DetSet (DS), and two HalfRing (HR) *Planck* 353 GHz polarization maps (Planck Collaboration VII 2015). The two HM maps are made from the two halves of the full-mission *Planck* data, whereas the two HR maps are produced by splitting each ring (also called stable pointing period) into two equal duration parts. The two DS maps are constructed using two subsets of polarization-sensitive bolometers at a given frequency. The noise is uncorrelated between the two HM, HR, and DS maps. We only use them to compute the error bars on the relevant quantities that we measure in this paper.

The total polarization intensity ( $P_{353}$ ) and the polarization angle ( $\psi$ ) are derived from the full-mission Stokes  $Q_{353}$  and  $U_{353}$

<sup>1</sup> *Planck* (<http://www.esa.int/Planck>) is a project of the European Space Agency (ESA) with instruments provided by two scientific consortia funded by ESA member states and led by Principal Investigators from France and Italy, telescope reflectors provided through a collaboration between ESA and a scientific consortium led and funded by Denmark, and additional contributions from NASA (USA).

maps at 353 GHz using the relations

$$P_{353} = \sqrt{Q_{353}^2 + U_{353}^2}, \quad (1)$$

$$\psi = 0.5 \times \text{atan2}(-U_{353}, Q_{353}), \quad (2)$$

where the two-argument function  $\text{atan2}(-U_{353}, Q_{353})$  is used to compute  $\text{atan}(-U_{353}/Q_{353})$  avoiding the  $\pi$  ambiguity. To recover the correct full range of polarization angles ( $[-\pi/2, \pi/2]$  as used for  $\psi$  here), attention must be paid to the signs of both  $U_{353}$  and  $Q_{353}$ , not just their ratio. We use the IAU convention for  $\psi$ , which is measured from the Galactic North (GN) and positive to the East. The minus sign in Eq. (2) converts the convention provided in the *Planck* data to that of the IAU (see [Planck Collaboration Int. XIX 2015](#)). The orientation angle ( $\chi$ ) of  $\mathbf{B}_{\text{POS}}$  is defined within the  $\pi$  ambiguity by adding  $\pi/2$  to the polarization angle

$$\chi = \psi + \frac{\pi}{2}. \quad (3)$$

For the dust intensity at 353 GHz, we use the model map  $D_{353}$ , computed from a modified blackbody fit to the *Planck* data at  $\nu \geq 353$  GHz and the IRAS 100  $\mu\text{m}$  map ([Planck Collaboration XI 2014](#)). This map has lower noise than the 353 GHz Stokes *I* map and is corrected for zodiacal light emission, CMB anisotropies, and the cosmic infrared background monopole. We neglect the contribution of the CMB polarization at 353 GHz for this study.

The full-mission *Planck* Stokes  $Q_{353}$  and  $U_{353}$  maps are provided in HEALPix<sup>2</sup> format ([Górski et al. 2005](#)) at 4'8 resolution and  $D_{353}$  at 5'. To increase the signal-to-noise ratio, we smooth the three maps to a common resolution of 15', taking into account the effective beam response of each map, and reduce to a HEALPix resolution of  $N_{\text{side}} = 512$ . For the polarization data, we decompose the Stokes  $Q_{353}$  and  $U_{353}$  maps into  $E_{353}$  and  $B_{353}$   $a_{\ell m}$ s ( $E_{\ell m}$  and  $B_{\ell m}$ ) using the “ianafast” routine of HEALPix, apply the Gaussian smoothing in harmonic space (after deconvolving the effective azimuthally symmetric beam response of each map), and transform the smoothed  $E_{353}$  and  $B_{353}$   $a_{\ell m}$ s back to  $Q_{353}$  and  $U_{353}$  maps using the “isynfast” routine at  $N_{\text{side}} = 512$ . We also transform the  $E_{353}$  and  $B_{353}$   $a_{\ell m}$ s to  $E_{353}$  and  $B_{353}$  maps at  $N_{\text{side}} = 512$  using the relations

$$E_{353}(\hat{\mathbf{n}}) = \sum E_{\ell m} Y_{\ell m}(\hat{\mathbf{n}}), \quad B_{353}(\hat{\mathbf{n}}) = \sum B_{\ell m} Y_{\ell m}(\hat{\mathbf{n}}). \quad (4)$$

All the maps that we use are in thermodynamic units ( $\mu\text{K}_{\text{CMB}}$ ).

In this paper, we work with the bandpass-filtered dust intensity map,  $D_{353}^{\text{b}}$ , to identify and isolate filaments over the filtering scale using a filament-finding algorithm. By filtering out large-scale and small-scale modes, we enhance the contrast of the filaments with respect to the diffuse background and reduce the instrumental noise, which is critical for accurately measuring the polarization orientations of the filaments within regions of low column density at high Galactic latitude.

For filtering, we apply the three-dimensional spline wavelet decomposition based on the undecimated wavelet transform, as described by [Starck et al. \(2006\)](#). We use the publicly available package Interactive Sparse Astronomical Data Analysis Packages (ISAP<sup>3</sup>) to compute the  $D_{353}^{\text{b}}$  map at  $N_{\text{side}} = 512$  resolution. The spline wavelet used in this analysis provides less oscillation in position space compared to Meyers or needlet ones ([Lanusse et al. 2012](#)). The filtering is done in pixel space; the corresponding bandpass filter in harmonic space varies a little

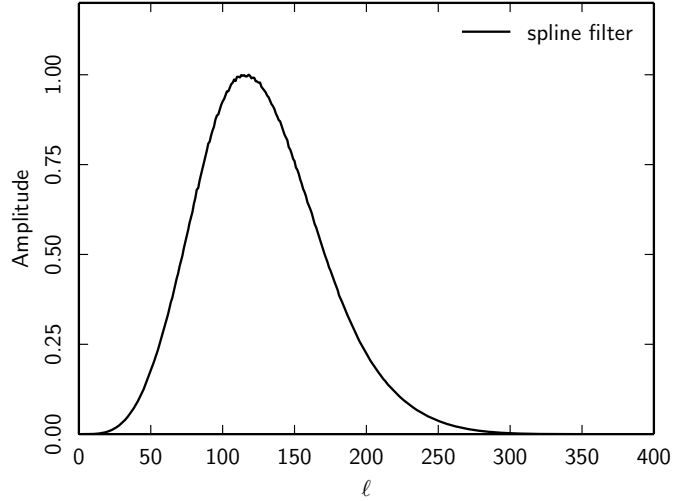


**Fig. 1.** The representative bandpass filter, retaining only the scales between  $\ell = 30$  and 300.

over the sky. Figure 1 presents the typical shape of this bandpass filter, which selects the scales between  $\ell = 30$  and 300. The filtering scale is chosen in such a way that it highlights all the bright filaments present in the *Planck*  $D_{353}$  map. We also compute the bandpass-filtered polarization maps,  $Q_{353}^{\text{b}}$ ,  $U_{353}^{\text{b}}$ ,  $E_{353}^{\text{b}}$ , and  $B_{353}^{\text{b}}$ .

### 3. Filament-finding algorithm

#### 3.1. Methodology

Identification of filaments as coherent structures is a crucial part of this analysis. Previous studies used algorithms such as DisPerSE ([Sousbie 2011](#); [Arzoumanian et al. 2011](#)), getfilaments ([Men'shchikov 2013](#)), and the rolling Hough transform ([Clark et al. 2014](#)). [Hennebelle \(2013\)](#) and [Soler et al. \(2013\)](#) used the inertia matrix and the gradient of the density and column density fields to identify filaments in numerical simulations of MHD turbulence.

In this paper, we employ the Smoothed Hessian Major Axis Filament Finder (SMAFF, [Bond et al. 2010a](#)) algorithm, which has been used to identify filaments in the three-dimensional galaxy distribution ([Bond et al. 2010b](#)). SMAFF is primarily based on the Hessian analysis. The Hessian analysis has also been used to analyse the *Planck* dust total intensity map in [Planck Collaboration Int. XXXII \(2014\)](#), *Herschel* images of the L1641 cloud in Orion A ([Polychroni et al. 2013](#)), and large-scale structure in simulations of the cosmic web ([Colombi et al. 2000](#); [Forero-Romero et al. 2009](#)). [Planck Collaboration Int. XXXII \(2014\)](#) has reported good agreement between the filament orientations derived from the Hessian and inertia matrix algorithms.

#### 3.2. Implementation

In this study, we apply the two-dimensional version of SMAFF to the  $D_{353}^{\text{b}}$  map, which is shown in the upper right panel of Fig. 2. From the Hessian matrix, we compute an all-sky map of the lower eigenvalue  $\lambda_-$  and the orientation angle  $\theta_-$  of the perpendicular to the corresponding eigenvector, measured with respect to the GN. The details of the Hessian analysis are provided in Appendix A. The map of  $\lambda_-$  is presented in the lower left panel of Fig. 2. For the subsequent analysis, we consider

<sup>2</sup> <http://healpix.jpl.nasa.gov>

<sup>3</sup> <http://www.cosmostat.org/isap.html>

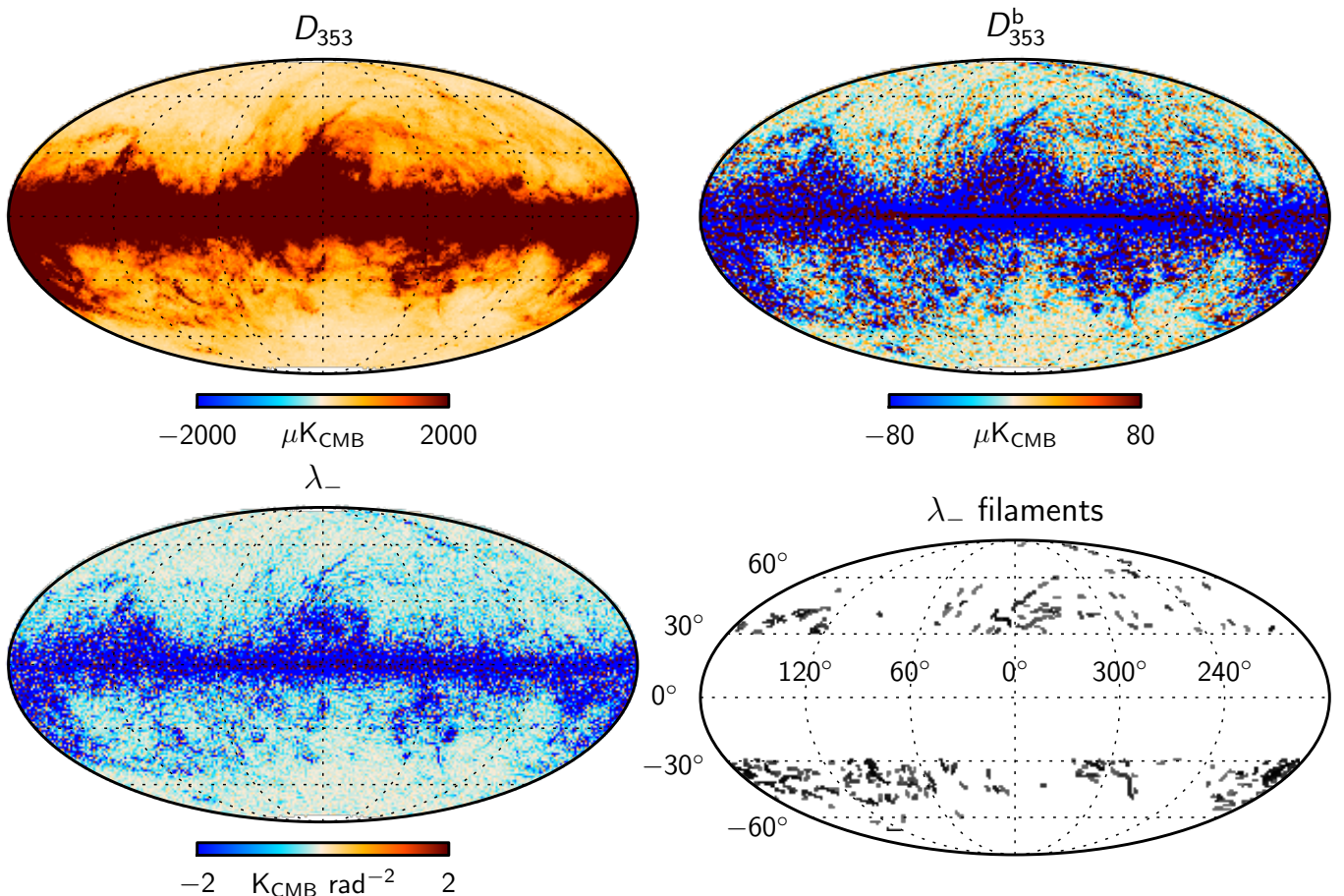


**Fig. 2.** Data processing steps implemented to identify filaments from the *Planck* data. We start with the *Planck*  $D_{353}$  map (upper left panel) smoothed at  $15'$  resolution. The bandpass-filtered  $D_{353}^b$  map (upper right panel) is produced using the spline wavelet decomposition, retaining only the scales between  $\ell = 30$  and  $300$ . The lower eigenvalue map of the Hessian matrix,  $\lambda_-$ , is shown in the lower left panel. Structures identified in the high-latitude sky  $\lambda_-$  map are shown in the lower right panel. The superimposed graticule is plotted in each image and labelled only on the lower right panel. It shows lines of constant longitude separated by  $60^\circ$  and lines of constant latitude separated by  $30^\circ$ . The same graticule is used in all plots of the paper.

only the high-latitude sky, defined as  $|b| > 30^\circ$ , with the Large Magellanic Cloud and Small Magellanic Cloud regions masked out.

The map of  $\lambda_-$  highlights filaments in the  $D_{353}^b$  map with an orientation angle  $\theta_-$ , which we refer to as the Hessian angle hereafter. The distribution of  $\lambda_-$  over the unmasked pixels is shown in Fig. 3. This distribution of  $\lambda_-$  is non-Gaussian with an extended tail. We use the median absolute deviation (MAD, Hampel 1974; Komm et al. 1999) to measure the width,  $\sigma_{\lambda_-}$ , of the distribution, as given by

$$\sigma_{\lambda_-} = 1.4826 \times \text{median}(|\lambda_- - m_{\lambda_-}|), \quad (5)$$

where  $m_{\lambda_-}$  is the median of the  $\lambda_-$  distribution. We select filaments using an upper threshold ( $K_-$ ) on  $\lambda_-$  given by

$$K_- = m_{\lambda_-} - 3\sigma_{\lambda_-}. \quad (6)$$

Hereafter, we refer to the filaments satisfying  $\lambda_- < K_-$  as “strong”. This threshold  $K_-$  separates the strong filaments from the weak ones, as detailed in Appendices B and C. By construction, the threshold  $K_-$  rejects pixels where  $\lambda_-$  is positive, since those pixels do not correspond to local maxima.

We seek coherent elongated structures in the map. In SMAFF, this is achieved by placing an upper limit  $C$  on the difference

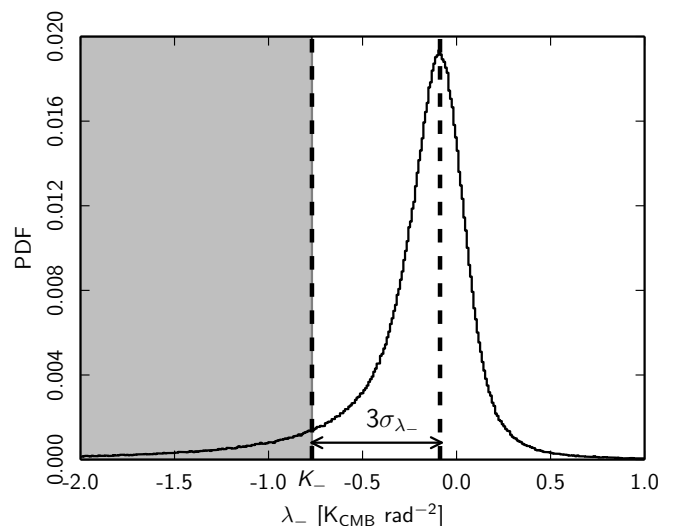


**Fig. 3.** Distribution of the eigenvalues  $\lambda_-$  over the unmasked pixels in the high-latitude sky. The grey region represents the pixels that were used in the SMAFF algorithm to find strong filaments.

between Hessian angles within a given structure. For our purpose, we set the value of  $C = 15^\circ$  to identify relatively straight filaments.

We start with the pixel having the most negative  $\lambda_-$  and denote the corresponding Hessian orientation angle by  $\theta_-^s$ . We identify its neighbouring pixels using the “neighbours\_ring” routine of HEALPix and look for pixels with  $\lambda_- < K_-$  and orientation angle such that  $|\theta_- - \theta_-^s| \leq C$ . If both conditions are satisfied, we count that neighbouring pixel as a part of the filament and move on to that neighbouring pixel. The neighbouring pixel becomes the new reference point and we search for its neighbours that satisfy both conditions. In our algorithm,  $\theta_-^s$  is fixed by the starting pixel, which has the most negative  $\lambda_-$ . We continue this friend-of-friend algorithm to connect pixels until one of the conditions is no longer satisfied. We limit our selection to filaments with a length ( $L$ , defined as the maximum angular distance between pixels within a given structure) larger than or equal to the threshold length  $L_0$ , which we choose to be  $2^\circ$ . This process yields a set of 259 elongated filaments, as shown in the lower left panel of Fig. 2. Hereafter, we refer to this set as our filament sample. Selected sky pixels represent 2.2 % of the high-latitude sky considered in our analysis. There is no overlap between the filaments in our sample.

The column density is computed from the  $D_{353}^b$  map using the conversion factor,  $0.039 \text{ MJy sr}^{-1}$  per  $10^{20} \text{ H cm}^{-2}$ ; this was derived in Planck Collaboration Int. XVII (2014) by correlating the Planck 353 GHz dust total emission map with an HI column density map over the southern Galactic polar cap. We average the column density along each filament and assign one mean column density,  $\bar{N}_H^b$ , to each. This column density is computed on the filtered intensity map. The histogram of  $\bar{N}_H^b$  for the filament sample is presented in Fig. 4. The number of filaments per  $\bar{N}_H^b$  is represented by  $N_F$ .

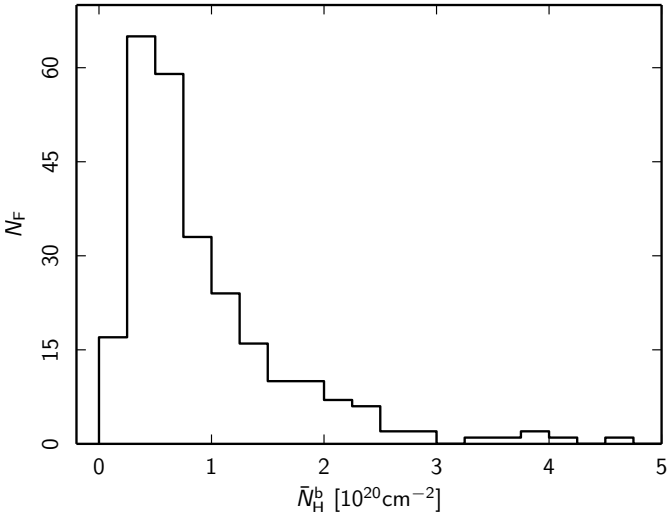


**Fig. 4.** Histogram of the mean column density of the filament sample. The column density is computed from the  $D_{353}^b$  map using the conversion factor derived in Planck Collaboration Int. XVII (2014).

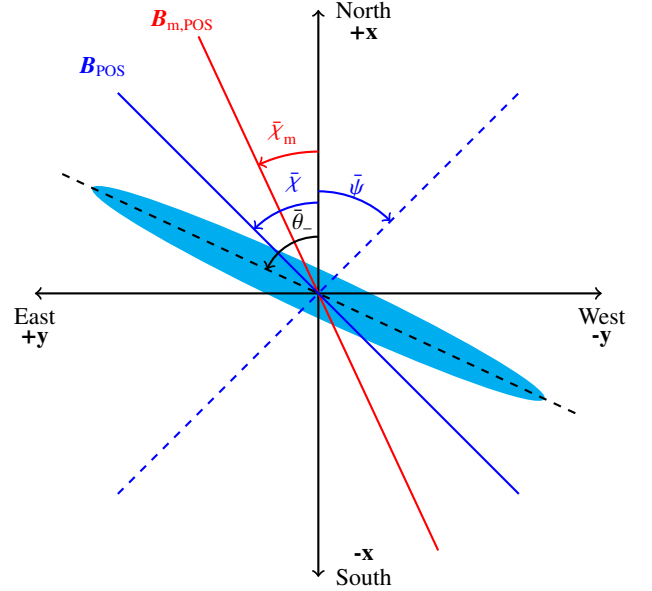


**Fig. 5.** Sketch of the mean orientation angle of the filament ( $\bar{\theta}_-$ ), the magnetic field ( $\bar{\chi}$ ), the polarization angle ( $\bar{\psi}$ ), and the large-scale GMF ( $\bar{\chi}_m$ ) along the filament. All the angles are defined with respect to the GN and follow the IAU convention.

#### 4. Interplay between the filament orientation and the magnetic field

In this section, we study the orientations of matter structures and  $B_{\text{POS}}$  in our filament sample (Sect. 3). The orientation angle of  $B_{\text{POS}}$  is derived from the observed Stokes  $Q_{353}$  and  $U_{353}$  maps using Eqs. (2) and (3). We also consider the orientation angle ( $\chi_m$ ) of  $B_{m,\text{POS}}$ , as estimated from starlight polarization observations (Heiles 1996) and pulsar rotation measures (Rand & Lyne 1994; Han et al. 1999). We compare these three orientations, as represented in Fig. 5. Our analysis follows Planck Collaboration Int. XXXII (2014), which used a set of pixels representing approximately 4 % of the sky at low and intermediate Galactic latitudes. Only 25 % of the pixels in our current filament sample were considered in this earlier study.

##### 4.1. Relative orientation of the filaments and the magnetic field

We study the angle difference between the orientations of the filaments and  $B_{\text{POS}}$  in our sample. First we associate one POS orientation angle with each of the filaments with respect to the GN. By construction, due to our selection criteria on the angles, the filaments are fairly straight and, hence, they may be described with a single orientation angle. Given one filament, we measure the mean orientation angle,  $\bar{\theta}_-$ , over the  $n$  pixels that belongs to it. We make use of the pseudo-vector field with unit length computed from the values of  $\theta_-$  for each pixel. This pseudo-vector has components  $Q_- = \cos 2\theta_-$  and  $U_- = -\sin 2\theta_-$  (following the HEALPix convention for the  $Q_-$  and  $U_-$  components). The mean POS orientation angle  $\bar{\theta}_-$  of the filament is obtained by first averaging  $Q_-$  and  $U_-$  over all  $n$  pixels and then calculating the position angle of this averaged pseudo-vector. It is given by

$$\bar{\theta}_- = 0.5 \times \text{atan2} \left( -\frac{1}{n} \sum_{i=1}^n U_-, \frac{1}{n} \sum_{i=1}^n Q_- \right). \quad (7)$$

If we rotate the Stokes  $Q_{353}$  and  $U_{353}$  maps by  $\bar{\theta}_-$ , i.e., into the frame where the axis of the filament is in the North-South direction, the rotated  $Q_{353}$  and  $U_{353}$  can be written as

$$Q'_{353} = Q_{353} \cos 2\bar{\theta}_- - U_{353} \sin 2\bar{\theta}_-, \quad (8)$$

$$U'_{353} = Q_{353} \sin 2\bar{\theta}_- + U_{353} \cos 2\bar{\theta}_-. \quad (9)$$

Combining Eqs. (8) and (9) with Eqs. (1) and (2), we get

$$Q'_{353} = P_{353} \cos 2(\psi - \bar{\theta}_-) = -P_{353} \cos 2(\chi - \bar{\theta}_-), \quad (10)$$

$$U'_{353} = -P_{353} \sin 2(\psi - \bar{\theta}_-) = P_{353} \sin 2(\chi - \bar{\theta}_-), \quad (11)$$

where the orientation angle  $\chi$  is defined in Eq. (3). Similar to the computation of  $\bar{\theta}_-$ , we average  $Q'_{353}$  and  $U'_{353}$  over all  $n$  pixels and then calculate the position angle of this averaged pseudo-vector

$$\bar{Q}'_{353} = \frac{1}{n} \sum_{i=1}^n Q'_{353} \equiv -\bar{P}_{353} \cos 2\Delta_{\bar{\chi}-\bar{\theta}_-}, \quad (12)$$

$$\bar{U}'_{353} = \frac{1}{n} \sum_{i=1}^n U'_{353} \equiv \bar{P}_{353} \sin 2\Delta_{\bar{\chi}-\bar{\theta}_-}, \quad (13)$$

where

$$\Delta_{\bar{\chi}-\bar{\theta}_-} = 0.5 \times \text{atan2}(\bar{U}'_{353}, -\bar{Q}'_{353}), \quad (14)$$

$$\bar{P}_{353} = \sqrt{\bar{Q}'_{353}{}^2 + \bar{U}'_{353}{}^2}. \quad (15)$$

The angle difference  $\Delta_{\bar{\chi}-\bar{\theta}_-}$  measures the weighted mean of the angle difference per pixel between the orientations of the given filament and  $\mathbf{B}_{\text{POS}}$ . The index  $\bar{\chi}$  refers to the mean orientation angle of  $\mathbf{B}_{\text{POS}}$  along the filament. Note that we directly measure the angle difference between the filament and  $\mathbf{B}_{\text{POS}}$ , without computing  $\bar{\chi}$  for each filament.

The histogram of relative orientation (HRO) between the filament and  $\mathbf{B}_{\text{POS}}$  for our filament sample is presented in the upper panel of Fig. 6. The mean value of the histogram is  $2^\circ.3$  computed using the equivalent of Eq. (7). Our histogram agrees with the pixel-by-pixel analysis at intermediate and low Galactic latitudes presented in Planck Collaboration Int. XXXII (2014). Like in this earlier study, we find that the filaments are statistically aligned with  $\mathbf{B}_{\text{POS}}$ . A similar alignment between the filaments in the intensity map and  $\mathbf{B}_{\text{POS}}$  has been reported for synchrotron emission observed by WMAP at 23 GHz (Vidal et al. 2015).

To quantify the shape of the histogram of  $\Delta_{\bar{\chi}-\bar{\theta}_-}$ , we fit it with a Gaussian plus a constant. The Gaussian has a  $1\sigma$  dispersion of  $19^\circ$ . The constant may be accounted for by the projection of the magnetic field and filament orientations on the POS as discussed in Planck Collaboration Int. XXXII (2014).

#### 4.2. Relative orientation of the magnetic field and the large-scale Galactic magnetic field

Here, we compare the orientation of  $\mathbf{B}_{\text{POS}}$  on the filaments with that of  $\mathbf{B}_{\text{m,POS}}$ . Heiles (1996) derived the orientation of  $\mathbf{B}_{\text{m,POS}}$  pointing towards  $l_0 = 82^\circ.8 \pm 4^\circ.1$  and  $b_0 = 0^\circ.4 \pm 0^\circ.5$  from the polarization pseudo-vectors of stars more distant than 500 parsecs. Slightly different  $l_0$  values have been reported in other studies. From the rotation measures of nearby pulsars within a few hundred parsecs of the Sun, Rand & Lyne (1994) found the direction of  $\mathbf{B}_{\text{m,POS}}$  pointing towards  $l_0 = 88^\circ \pm 5^\circ$ . In another study of pulsar rotation measures, Han et al. (1999) derived the direction of  $\mathbf{B}_{\text{m,POS}}$  as  $l_0 \simeq 82^\circ$ . These two studies do not report

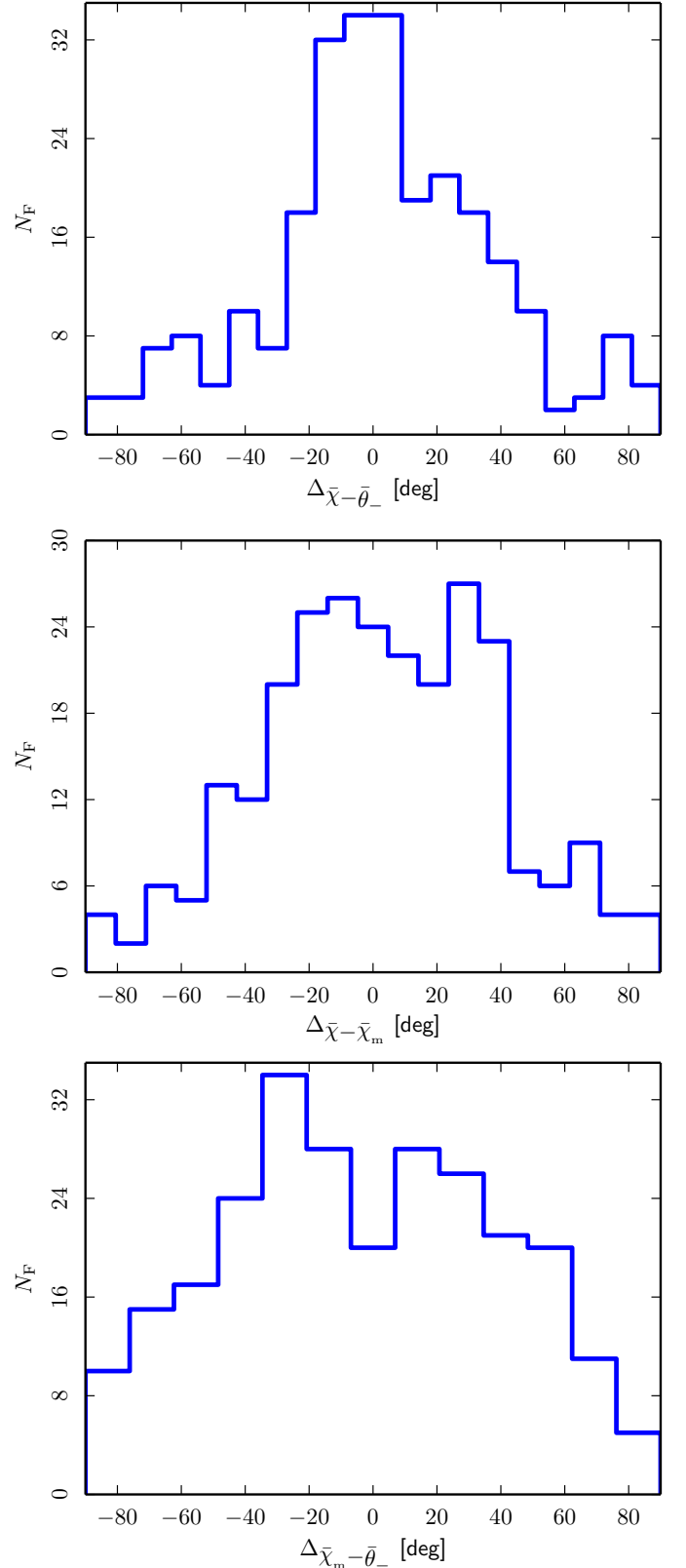


**Fig. 6.** Upper panel: HRO between the filaments and  $\mathbf{B}_{\text{POS}}$ . Middle panel: HRO between  $\mathbf{B}_{\text{POS}}$  and  $\mathbf{B}_{\text{m,POS}}$ . Lower panel: HRO between the filaments and  $\mathbf{B}_{\text{m,POS}}$ .

values for  $b_0$ , which is assumed to be zero. Based on these observations, we assume that the mean orientation of  $\mathbf{B}_{\text{m,POS}}$  in the

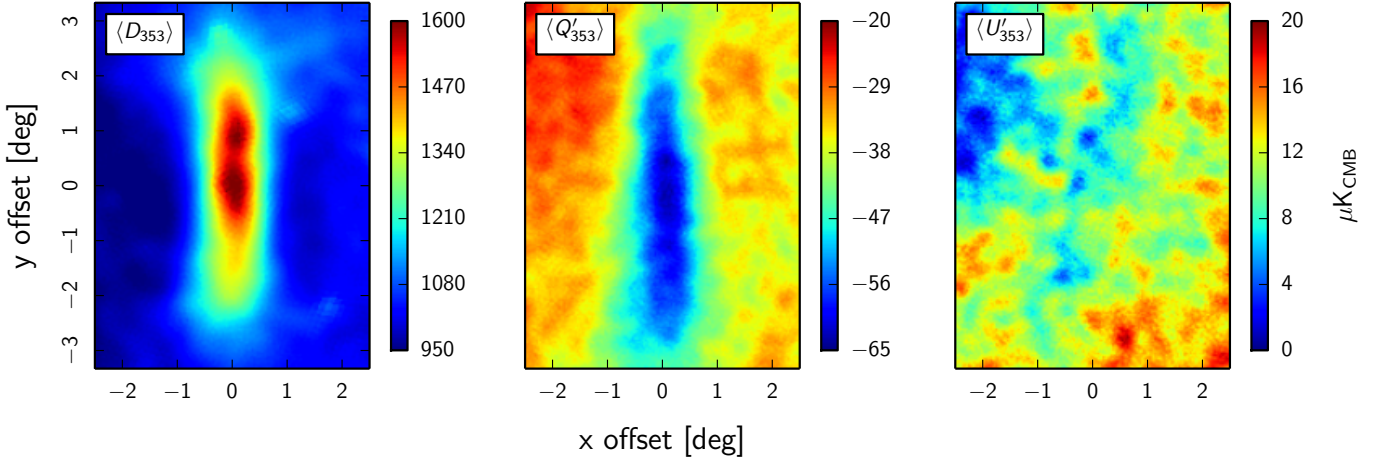


**Fig. 7.** Mean images of the *Planck*  $\langle D_{353} \rangle$ ,  $\langle Q'_{353} \rangle$ , and  $\langle U'_{353} \rangle$  maps over the  $\lambda_-$  filaments at  $15'$  resolution.

solar neighbourhood is  $l_0 = 84^\circ \pm 10^\circ$  and  $b_0 = 0^\circ \pm 10^\circ$ , with the same uncertainty on  $l_0$  and  $b_0$ .

We construct a pseudo-vector field with unit length based on the uniform orientation of  $\mathbf{B}_{\text{m,POS}}$ . This pseudo-vector has components:  $Q_{\text{m}} = \cos 2\psi_{\text{m}} = \cos 2(\chi_{\text{m}} - \pi/2)$  and  $U_{\text{m}} = -\sin 2\psi_{\text{m}} = -\sin 2(\chi_{\text{m}} - \pi/2)$  (following the HEALPix convention for the  $Q_{\text{m}}$  and  $U_{\text{m}}$  maps), where  $\psi_{\text{m}}$  is the polarization angle of  $\mathbf{B}_{\text{m,POS}}$ . The procedure to go from the uniform  $\mathbf{B}_{\text{m,POS}}$  pointing towards  $(l_0, b_0)$  to  $\psi_{\text{m}}$  is detailed by Heiles (1996). The mean orientation angle  $\langle \bar{\chi}_{\text{m}} \rangle$  of  $\mathbf{B}_{\text{m,POS}}$  for each filament is obtained by first averaging  $Q_{\text{m}}$  and  $U_{\text{m}}$  over all  $n$  pixels within a filament and then calculating the position angle of this averaged pseudo-vector. We compute the angle difference,  $\Delta_{\bar{\chi}-\bar{\chi}_{\text{m}}}$ , between the orientations of  $\mathbf{B}_{\text{POS}}$  and  $\mathbf{B}_{\text{m,POS}}$  on the filament in a similar manner to the method described in Sect. 4.1.

The HRO between  $\mathbf{B}_{\text{POS}}$  and  $\mathbf{B}_{\text{m,POS}}$  for our filament sample is presented in the middle panel of Fig. 6. The mean value of the histogram is  $1.3 \pm 3.7$  where the uncertainty is computed by changing the mean orientation of  $\mathbf{B}_{\text{m,POS}}$  within its quoted uncertainties. This HRO has a larger dispersion than that between the filaments and  $\mathbf{B}_{\text{POS}}$  shown in the upper panel of Fig. 6. To quantify the shape of the histogram of  $\Delta_{\bar{\chi}-\bar{\chi}_{\text{m}}}$ , we fit it with a Gaussian plus a constant. The Gaussian has a  $1\sigma$  dispersion of  $36^\circ$ .

We conclude that  $\mathbf{B}_{\text{POS}}$  of our filament sample is statistically aligned with  $\mathbf{B}_{\text{m,POS}}$ . Planck Collaboration Int. XXXII (2014) reports a similar correlation, for the low and intermediate Galactic latitudes, when comparing the polarization measured on the filaments with their background polarization maps. The scatter measured by the HRO may be interpreted considering both the turbulent component of the magnetic field and projection effects.

#### 4.3. Relative orientation of the large-scale Galactic magnetic field and the filaments

We combine the results obtained in Sects. 4.1 and 4.2 to assess statistically the orientation of  $\mathbf{B}_{\text{m,POS}}$  in the solar neighbourhood with respect to the filaments.  $\mathbf{B}_{\text{POS}}$  is statistically aligned with the filaments in our sample and with  $\mathbf{B}_{\text{m,POS}}$ . From both results, one would intuitively expect  $\mathbf{B}_{\text{m,POS}}$  to be statistically aligned with the filaments. To test this expectation, for each filament, we compute the angle difference,  $\Delta_{\bar{\chi}_{\text{m}}-\bar{\theta}_-}$ , between the orientations of  $\mathbf{B}_{\text{m,POS}}$  and the filament. The angle difference  $\Delta_{\bar{\chi}_{\text{m}}-\bar{\theta}_-}$  is computed in a similar manner to the method described in Sect. 4.1.

The HRO between the filament and  $\mathbf{B}_{\text{m,POS}}$  for our filament sample is presented in the lower panel of Fig. 6. A correlation between the orientation angles of the filament and  $\mathbf{B}_{\text{m,POS}}$  is present, but the HRO shows more scatter than the HRO between the filaments and  $\mathbf{B}_{\text{POS}}$  and that between  $\mathbf{B}_{\text{POS}}$  and  $\mathbf{B}_{\text{m,POS}}$ . The histogram has a mean value of  $-3.1 \pm 2.6$ . To quantify the shape of the histogram of  $\Delta_{\bar{\chi}-\bar{\chi}_{\text{m}}}$ , we fit with a Gaussian plus a constant. The Gaussian has a  $1\sigma$  dispersion of  $54^\circ$ . Planck Collaboration Int. XXXII (2014) reported a similar loss of correlation when comparing the orientations of the filaments with that of  $\mathbf{B}_{\text{POS}}$  derived from their local background polarization maps.

## 5. Mean polarization properties of filaments

In this section, we present stacked images of the filaments in Stokes  $I$ ,  $Q$ , and  $U$ , after rotation to align the filaments and to compute  $Q$  and  $U$  with respect to their orientation. The images are used to compute the average polarization fraction of our sample of filaments.

### 5.1. Stacking filaments

Over the high-latitude sky, the signal-to-noise ratio of the 353 GHz *Planck* polarization maps is low and it is not possible to measure the polarization fraction of individual dust intensity filaments in our sample. In order to increase the signal-to-noise ratio, we therefore stack images of the 259 filaments and their surroundings.

For each filament in the sample, using the “gnomview” routine of HEALPix, we extract from the *Planck* maps a local, flat-sky, image ( $7^\circ \times 5^\circ$  patch) centred on the filament centre and rotated by  $\bar{\theta}_-$  in the clockwise direction to align the filament in the North-South direction. We stack the images of the filaments in  $D_{353}$ ,  $Q'_{353}$ , and  $U'_{353}$  (as defined in Eqs. 8 and 9) after aligning all the maps in the North-South direction. We produce mean stacked images, denoted with angle brackets  $\langle \cdot \rangle$ , by dividing the sum of the individual images by the total number of filaments in our sample; they are presented in Fig. 7. The  $1\sigma$  errorbar both on the  $\langle Q'_{353} \rangle$  and  $\langle U'_{353} \rangle$  images is  $1.3 \mu\text{K}_{\text{CMB}}$ , as computed from the difference of two polarization HM maps. All the features presented in Fig. 7 are significant compared to the data systematics and statistical noise. The average filament appears as a negative feature with respect to the background in the  $\langle Q'_{353} \rangle$  image and is not seen in the  $\langle U'_{353} \rangle$  image. This result is a direct consequence

of the alignment between the filaments and  $\mathbf{B}_{\text{POS}}$  (Sect. 4.1 and Zaldarriaga 2001). The background in both the  $\langle Q'_{353} \rangle$  and  $\langle U'_{353} \rangle$  images is rather homogeneous. This reflects the smoothness of  $\mathbf{B}_{\text{POS}}$  within the  $7^\circ \times 5^\circ$  patches.

We perform a null test to assess the significance of the stacking of filaments. This test is made by stacking 259 randomly chosen  $7^\circ \times 5^\circ$  patches in the high-latitude sky. Each patch is rotated in the clockwise direction, with the orientation angle  $\theta_-$  of the central pixel. The images of  $\langle D_{353} \rangle$ ,  $\langle Q'_{353} \rangle$ , and  $\langle U'_{353} \rangle$  for random patches are consistent with noise. The amplitude of  $\langle Q'_{353} \rangle$  and  $\langle U'_{353} \rangle$  images is comparable to that of the difference between stacked images obtained when applying the same analysis to each of the two polarization HM maps. This confirms the hypothesis that the filaments detected in Fig. 7 are indeed real and are rotated with a well-determined angle  $\bar{\theta}_-$ .

## 5.2. Polarization fraction

Instead of using individual pixels, we collapse the mean stacked images in the filament direction to draw the radial profiles ( $R$ ) of the  $D_{353}$ ,  $Q'_{353}$ , and  $U'_{353}$  images, which are presented in Fig. 8. The shaded area in Fig. 8 represents the  $1\sigma$  dispersion from the data values at a given radial distance from the filament axis that we average. We clearly identify the profile of the filament on top of the constant background emission in the  $D_{353}$  and  $Q'_{353}$  radial profiles, while the radial profile of  $U'_{353}$  is consistent with a constant background emission. The radial profiles of  $D_{353}$ ,  $Q'_{353}$ , and  $U'_{353}$  can be decomposed into the filament (F) and the background (B) contributions as

$$R_{D_{353}} = R_{D_{353}^{\text{F}}} + R_{D_{353}^{\text{B}}}, \quad (16)$$

$$R_{Q'_{353}} = R_{Q'_{353}^{\text{F}}} + R_{Q'_{353}^{\text{B}}}, \quad (17)$$

$$R_{U'_{353}} = R_{U'_{353}^{\text{F}}} + R_{U'_{353}^{\text{B}}}. \quad (18)$$

We fit the radial profiles of  $D_{353}$  and  $Q'_{353}$  in Fig. 8 with a Gaussian profile for the filament emission plus a constant for the background emission. We find that the centre of the Gaussian profile is zero and that their  $1\sigma$  dispersion is  $27' \pm 1'$  for both the  $D_{353}$  and  $Q'_{353}$  radial profiles.

Following Eqs. (12) and (13), we can express the average Stokes  $Q'_{353}$  and  $U'_{353}$  for one given filament as

$$\bar{Q}'_{353}^{\text{F}} = -\bar{P}_{353}^{\text{F}} \cos 2\Delta_{\bar{\chi}-\bar{\theta}_-}^{\text{F}} = -\bar{p}^{\text{F}} \bar{D}_{353}^{\text{F}} \cos 2\Delta_{\bar{\chi}-\bar{\theta}_-}^{\text{F}}, \quad (19)$$

$$\bar{U}'_{353}^{\text{F}} = \bar{P}_{353}^{\text{F}} \sin 2\Delta_{\bar{\chi}-\bar{\theta}_-}^{\text{F}} = \bar{p}^{\text{F}} \bar{D}_{353}^{\text{F}} \sin 2\Delta_{\bar{\chi}-\bar{\theta}_-}^{\text{F}}, \quad (20)$$

where  $\bar{D}_{353}^{\text{F}}$  and  $\bar{P}_{353}^{\text{F}}$  are the average specific intensity and polarization intensity of the filament. The superscript F represents the contribution from the filament only. The polarization fraction ( $\bar{p}^{\text{F}}$ ) of a filament is defined by

$$\bar{p}^{\text{F}} = \frac{\bar{P}_{353}^{\text{F}}}{\bar{D}_{353}^{\text{F}}}. \quad (21)$$

From Fig. 4, we know that most filaments in our sample have comparable column densities and hence roughly the same  $\bar{D}_{353}^{\text{F}}$ . The mean stacked Stokes  $\bar{Q}'_{353}^{\text{F}}$  and  $\bar{U}'_{353}^{\text{F}}$  values for all the filaments can be approximated as

$$\langle \bar{Q}'_{353}^{\text{F}} \rangle \simeq -\langle \bar{p}^{\text{F}} \cos 2\Delta_{\bar{\chi}-\bar{\theta}_-}^{\text{F}} \rangle \langle \bar{D}_{353}^{\text{F}} \rangle \simeq -\langle \bar{p}^{\text{F}} \rangle \langle \cos 2\Delta_{\bar{\chi}-\bar{\theta}_-}^{\text{F}} \rangle \langle \bar{D}_{353}^{\text{F}} \rangle, \quad (22)$$

$$\langle \bar{U}'_{353}^{\text{F}} \rangle \simeq \langle \bar{p}^{\text{F}} \sin 2\Delta_{\bar{\chi}-\bar{\theta}_-}^{\text{F}} \rangle \langle \bar{D}_{353}^{\text{F}} \rangle \simeq \langle \bar{p}^{\text{F}} \rangle \langle \sin 2\Delta_{\bar{\chi}-\bar{\theta}_-}^{\text{F}} \rangle \langle \bar{D}_{353}^{\text{F}} \rangle, \quad (23)$$

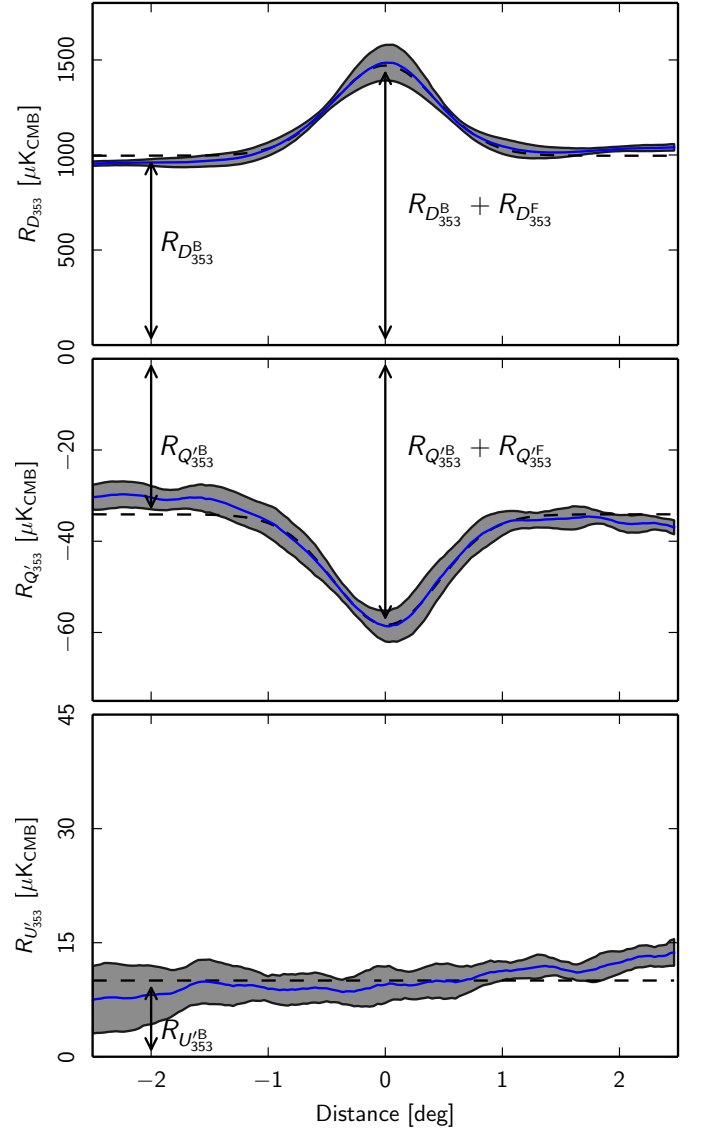


**Fig. 8.** Radial profiles of the mean stacked *Planck*  $D_{353}$ ,  $Q'_{353}$ , and  $U'_{353}$  images as functions of distance from the centre of the filament (blue line). The grey shaded region shows the  $1\sigma$  dispersion from the data values at a given radial distance from the filament axis that we average. The dashed line is the Gaussian fit to the filament profile plus a constant background emission.

where  $\langle \bar{p}^{\text{F}} \rangle$  is the mean polarization fraction of our filament sample. For the radial profiles of the filament emission, we have

$$R_{Q'_{353}^{\text{F}}} \simeq -\langle \bar{p}^{\text{F}} \rangle \langle \cos 2\Delta_{\bar{\chi}-\bar{\theta}_-}^{\text{F}} \rangle R_{D_{353}^{\text{F}}}, \quad (24)$$

$$R_{U'_{353}^{\text{F}}} \simeq \langle \bar{p}^{\text{F}} \rangle \langle \sin 2\Delta_{\bar{\chi}-\bar{\theta}_-}^{\text{F}} \rangle R_{D_{353}^{\text{F}}}. \quad (25)$$

The angle difference between the filaments and  $\mathbf{B}_{\text{POS}}$  (Eq. 14) is used for  $\Delta_{\bar{\chi}-\bar{\theta}_-}^{\text{F}}$ . The histogram of  $\Delta_{\bar{\chi}-\bar{\theta}_-}^{\text{F}}$  is roughly symmetric around  $0^\circ$ , implying  $R_{U'_{353}^{\text{F}}} \ll R_{Q'_{353}^{\text{F}}}$ .

Similarly, the radial profiles from the background emission can be written as

$$R_{Q'_{353}^{\text{B}}} \simeq -\langle \bar{p}^{\text{B}} \rangle \langle \cos 2\Delta_{\bar{\chi}-\bar{\theta}_-}^{\text{B}} \rangle R_{D_{353}^{\text{B}}}, \quad (26)$$

$$R_{U'_{353}^{\text{B}}} \simeq \langle \bar{p}^{\text{B}} \rangle \langle \sin 2\Delta_{\bar{\chi}-\bar{\theta}_-}^{\text{B}} \rangle R_{D_{353}^{\text{B}}}, \quad (27)$$



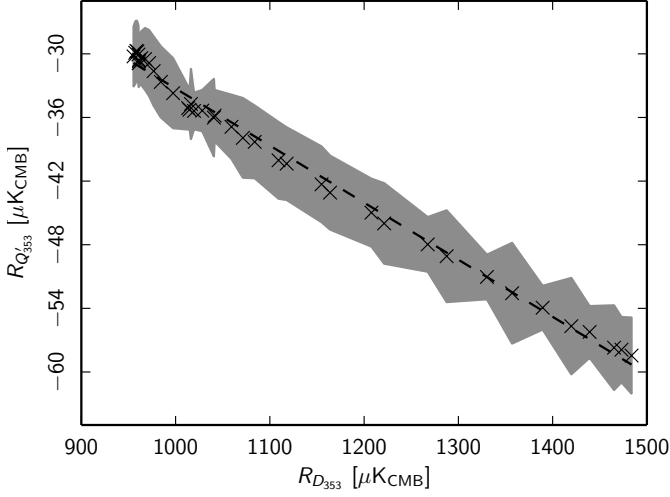


**Fig. 9.** Linear fit (dashed line) to the correlation between the mean radial profiles of the stacked  $Q'_{353}$  and  $D_{353}$  images. The grey shaded region shows the  $1\sigma$  dispersion from the data values at a given radial distance from the filament axis that we average.

where  $\langle \bar{p}^B \rangle$  is the average polarization fraction of the background emission and  $\Delta_{\chi-\bar{\theta}_-}^B$  is the angle difference between a given filament and  $\mathbf{B}_{\text{POS}}$  from its local background polarization.

The observed radial profile of the stacked  $Q'_{353}$  image in Fig. 8 can be written as

$$\begin{aligned} R_{Q'_{353}} &= R_{Q'_{353}^F} + R_{Q'_{353}^B} \\ &\simeq -\langle \bar{p}^F \rangle \langle \cos 2\Delta_{\chi-\bar{\theta}_-}^F \rangle R_{D_{353}^F} - \langle \bar{p}^B \rangle \langle \cos 2\Delta_{\chi-\bar{\theta}_-}^B \rangle R_{D_{353}^B} \\ &= -\langle \bar{p}^F \rangle \langle \cos 2\Delta_{\chi-\bar{\theta}_-}^F \rangle R_{D_{353}^F} \\ &\quad + \left[ \langle \bar{p}^F \rangle \langle \cos 2\Delta_{\chi-\bar{\theta}_-}^F \rangle - \langle \bar{p}^B \rangle \langle \cos 2\Delta_{\chi-\bar{\theta}_-}^B \rangle \right] R_{D_{353}^B} \\ &= a R_{D_{353}} + b, \end{aligned} \quad (28)$$

where  $a = -\langle \bar{p}^F \rangle \langle \cos 2\Delta_{\chi-\bar{\theta}_-}^F \rangle$  is the scaling parameter and  $b = \left[ \langle \bar{p}^F \rangle \langle \cos 2\Delta_{\chi-\bar{\theta}_-}^F \rangle - \langle \bar{p}^B \rangle \langle \cos 2\Delta_{\chi-\bar{\theta}_-}^B \rangle \right] R_{D_{353}^B}$  is the offset of the linear fit between the  $R_{Q'_{353}}$  and  $R_{D_{353}}$  profiles. The linear fit between  $R_{Q'_{353}}$  and  $R_{D_{353}}$  is shown in Fig. 9. The best-fit parameter values from the linear fit are

$$\langle \bar{p}^F \rangle \langle \cos 2\Delta_{\chi-\bar{\theta}_-}^F \rangle = 5.3\%, \quad (29)$$

$$\left[ \langle \bar{p}^F \rangle \langle \cos 2\Delta_{\chi-\bar{\theta}_-}^F \rangle - \langle \bar{p}^B \rangle \langle \cos 2\Delta_{\chi-\bar{\theta}_-}^B \rangle \right] R_{D_{353}^B} = 19.8 \mu\text{K}_{\text{CMB}}. \quad (30)$$

In our estimate of  $\langle \bar{p}^F \rangle \langle \cos 2\Delta_{\chi-\bar{\theta}_-}^F \rangle$ , the noise bias is negligible, because the noise averages out in the stacking of the  $Q'_{353}$  and  $U'_{353}$  maps. The HRO between the filament and  $\mathbf{B}_{\text{POS}}$  (upper panel in Fig. 6) is used to compute  $\langle \cos 2\Delta_{\chi-\bar{\theta}_-}^F \rangle$ , which is 0.48. Taking this factor into account, the mean polarization fraction of our filament sample is

$$\langle \bar{p}^F \rangle = 11\%. \quad (31)$$

We have computed  $\langle \bar{p}^F \rangle$  using the two independent subsets of the *Planck* data (HM maps). For both data sets, we find the same mean value of 11%. This is expected, because the HRO between the filaments and  $\mathbf{B}_{\text{POS}}$  is determined with high accuracy (Appendix D). It shows that the measurement error on  $\langle \bar{p}^F \rangle$

is small. Obviously  $\langle \bar{p}^F \rangle$  may be different for another set of filaments, because it depends on the angles of the filaments with respect to the plane of the sky.

The mean polarization fraction of the filaments determined from the filament sample is smaller than the maximum degree of polarization reported in [Planck Collaboration Int. XIX \(2015\)](#), which is  $p_{\text{max}} = 19.6\%$ . This result suggests that there is some depolarization due to changes in the magnetic field orientation within the filaments ([Planck Collaboration Int. XX 2015](#); [Planck Collaboration Int. XXXIII 2014](#)).

The offset  $b$  from the linear fit to the radial profiles of the  $Q'_{353}$  and  $D_{353}$  images is positive. This means that

$$\langle \bar{p}^B \rangle \langle \cos 2\Delta_{\chi-\bar{\theta}_-}^B \rangle < \langle \bar{p}^F \rangle \langle \cos 2\Delta_{\chi-\bar{\theta}_-}^F \rangle \quad (32)$$

The distribution of  $\Delta_{\chi-\bar{\theta}_-}^B$  for our filament sample is needed to compute  $\langle \bar{p}^B \rangle$ . We make a simple approximation using the HRO between the filament and  $\mathbf{B}_{\text{m,POS}}$  (lower panel in Fig. 6) as a proxy for  $\Delta_{\chi-\bar{\theta}_-}^B$ . We then find  $\langle \cos 2\Delta_{\chi-\bar{\theta}_-}^B \rangle = 0.25 \pm 0.14$  for our filament sample. Combining Eqs. (29) and (32), we put an upper limit on the mean polarization fraction of the background emission as

$$\langle \bar{p}^B \rangle < 21\%_{-7\%}^{+27\%}. \quad (33)$$

This upper limit on  $\langle \bar{p}^B \rangle$  depends on the mean orientation of  $\mathbf{B}_{\text{GMF}}$  and it ranges from 48% to 14% for the  $10^\circ$  uncertainty on  $l_0$  and  $b_0$  (Sect. 4.2). The profile of  $R_{U'_{353}^B}$  in the lower panel of Fig. 8 is roughly constant and positive. This result indicates that  $\mathbf{B}_{\text{POS}}$  is smooth within the  $7^\circ \times 5^\circ$  patches and  $\langle \sin 2\Delta_{\chi-\bar{\theta}_-}^B \rangle$  is positive (Eq. 27), which follows if the distribution of  $\Delta_{\chi-\bar{\theta}_-}^B$  is not symmetric with respect to  $0^\circ$ . We point out that the histogram in the lower panel in Fig. 6 may not be used to estimate the sign of  $\langle \sin 2\Delta_{\chi-\bar{\theta}_-}^B \rangle$  because the uncertainty on  $l_0$  and  $b_0$  is too large.

## 6. *E-B* asymmetry

In this section, we quantify the *E-B* asymmetry of dust polarization, over the  $\ell$  range 30 to 300, for our filament sample, and relate it to the relative orientation between filaments and  $\mathbf{B}_{\text{POS}}$ . First, we present the stacked images of filtered maps that we use to quantify the *E-B* asymmetry. Second, we compute the contribution of the pixels used in the stacking to the variance in the high-latitude sky. Last, we present an analytical approximation that relates the HRO between the filaments and  $\mathbf{B}_{\text{POS}}$  to the *E-B* asymmetry.

### 6.1. Stacked images of filtered maps

Here we use the *Planck*  $D_{353}^b$ ,  $Q_{353}^b$ ,  $U_{353}^b$ ,  $E_{353}^b$ , and  $B_{353}^b$  maps to analyse the  $\ell$  range, between 30 and 300, over which we identify the filaments in the dust intensity map. Our choice of  $\ell$  range has a large overlap with the angular scales,  $40 < \ell < 600$ , where the *E-B* asymmetry has been measured with the power spectra of dust polarisation. We stack all the bandpass-filtered maps, rotated by the mean orientation angle  $\bar{\theta}_-$  of the filament, as described in Sect. 5.1. The  $Q_{353}^b$  and  $U_{353}^b$  maps are the filtered Stokes  $Q_{353}$  and  $U_{353}$  maps computed with respect to the axis of the filament. The mean stacked images of the bandpass-filtered maps are presented in Fig. 10. The sidelobes that appear in the images of  $\langle D_{353}^b \rangle$ ,  $\langle Q_{353}^b \rangle$ , and  $\langle E_{353}^b \rangle$  of Fig. 10 on both sides of the filament centre are coming from the filtering. The  $1\sigma$  errorbar on the  $\langle Q_{353}^b \rangle$ ,  $\langle U_{353}^b \rangle$ ,  $\langle E_{353}^b \rangle$ , and  $\langle B_{353}^b \rangle$  images is

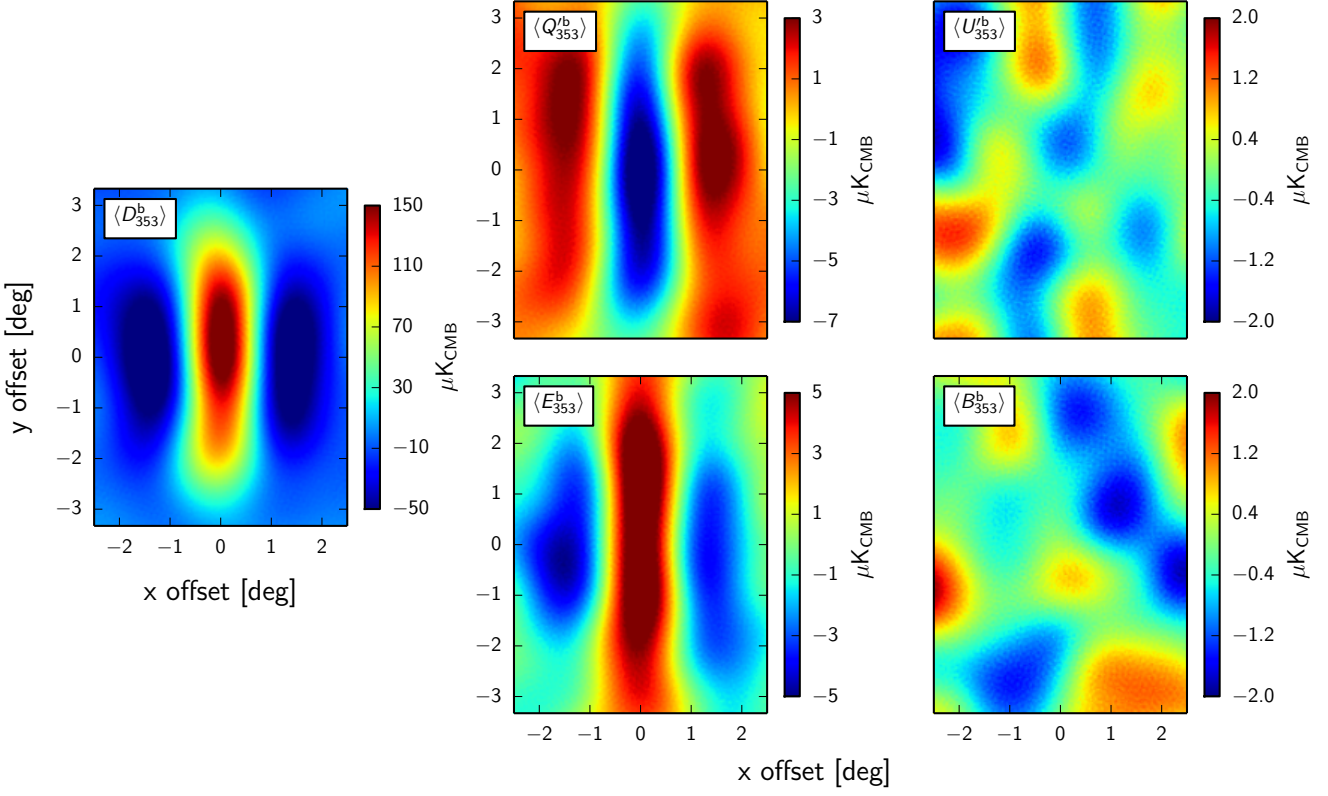


**Fig. 10.** Mean images of the *Planck*  $\langle D_{353}^b \rangle$ ,  $\langle Q_{353}^b \rangle$ ,  $\langle U_{353}^b \rangle$ ,  $\langle E_{353}^b \rangle$ , and  $\langle B_{353}^b \rangle$  maps over the  $\lambda_-$  filaments.

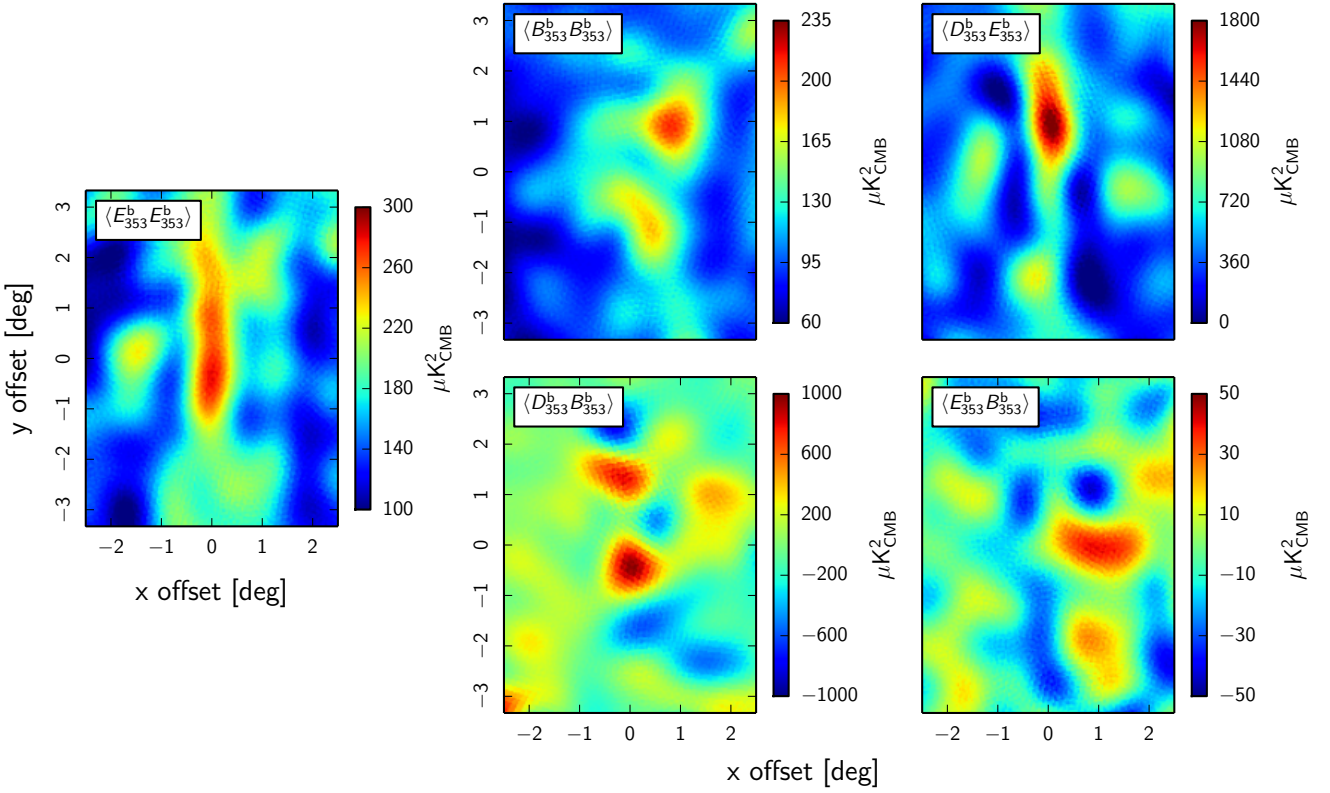


**Fig. 11.** Mean images of the *Planck*  $\langle E_{353}^b E_{353}^b \rangle$ ,  $\langle B_{353}^b B_{353}^b \rangle$ ,  $\langle D_{353}^b E_{353}^b \rangle$ ,  $\langle D_{353}^b B_{353}^b \rangle$ , and  $\langle E_{353}^b B_{353}^b \rangle$  maps over the  $\lambda_-$  filaments.

0.2  $\mu\text{K}_{\text{CMB}}$ , as computed from the difference of two polarization HM maps. The filaments appear as a negative feature in the  $\langle Q_{353}^b \rangle$  image and a positive feature in that of  $\langle E_{353}^b \rangle$ . The  $\langle U_{353}^b \rangle$  and  $\langle B_{353}^b \rangle$  images are consistent with a mean value zero.

Next, we stack the products of two quantities, i.e.,  $\langle D_{353}^b E_{353}^b \rangle$ ,  $\langle D_{353}^b B_{353}^b \rangle$ ,  $\langle E_{353}^b E_{353}^b \rangle$ ,  $\langle E_{353}^b B_{353}^b \rangle$ , and  $\langle B_{353}^b B_{353}^b \rangle$ . We follow the same methodology as discussed in Sect. 5.1 with oriented stacking at the centre of the filament. To avoid a noise bias in the square quantities,  $\langle E_{353}^b E_{353}^b \rangle$  and  $\langle B_{353}^b B_{353}^b \rangle$ , we compute the cross-product of the two HalfMission maps (HM1 and HM2). For other quantities,  $\langle D_{353}^b E_{353}^b \rangle$ ,  $\langle D_{353}^b B_{353}^b \rangle$ , and  $\langle E_{353}^b B_{353}^b \rangle$ , we use the full-mission maps. The images produced by stacking the products are presented in Fig. 11. Note that the maps shown in Figs. 10 and 11 are not used for data analysis, but still we comment on these images. We computed the mean stacked images from each of the two polarization DS or HR maps and all the features presented in Fig. 11 appear for both independent subset of *Planck* data. In the idealized description of the filaments in Zaldarriaga (2001), we will expect the average filament to appear similarly in the *EE*, *BB*, and *TE* maps. The differences between these three images shows that the reality of the dust sky is more complex than the idealized model.

## 6.2. Measured *E*-*B* asymmetry

We measure the *E*-*B* asymmetry at the filtering scale over the high-latitude (HL) region. We compute the variances ( $V$ ) of the  $E_{353}^b$  and  $B_{353}^b$  maps using the relations

$$V^{EE}(\text{HL}) = \frac{1}{N_{\text{HL}}} \sum_{i=1}^{N_{\text{HL}}} E_{353,\text{HM1}}^b E_{353,\text{HM2}}^b = (46.6 \pm 1.1) \mu\text{K}_{\text{CMB}}^2, \quad (34)$$

$$V^{BB}(\text{HL}) = \frac{1}{N_{\text{HL}}} \sum_{i=1}^{N_{\text{HL}}} B_{353,\text{HM1}}^b B_{353,\text{HM2}}^b = (29.1 \pm 1.0) \mu\text{K}_{\text{CMB}}^2, \quad (35)$$

where  $N_{\text{HL}}$  is the total number of pixels in the HL region. The ratio of the filtered  $B_{353}$  and  $E_{353}$  variances is

$$\frac{V^{BB}(\text{HL})}{V^{EE}(\text{HL})} = 0.62 \pm 0.03. \quad (36)$$

The uncertainty on  $V^{EE}$  is computed by repeating the calculation of Eq. (34) using the different cross-products, i.e., the two HalfRing (HR1 and HR2) and the two DetSet (DS1 and DS2) maps. We use the cross-HalfMissions as a reference for mean  $V^{EE}$ . The  $1\sigma$  uncertainty on  $V^{EE}$  comes from the differences of these cross-products (DetSets minus HalfMissions and HalfRings minus HalfMissions). This  $1\sigma$  uncertainty is dominated by data systematics rather than statistical noise. This is in agreement with the uncertainties on power spectra over the same  $\ell$  range, as shown for  $f_{\text{sky}} = 0.5$  in Figure 2 of Planck Collaboration Int. XXX (2014). The statistical noise on  $V^{EE}$  is estimated from the cross-HalfMissions between their two HalfRing half-differences,  $N^{EE} = (E_{353,\text{HR1}}^b - E_{353,\text{HR2}}^b)_{\text{HM1}}/2 \times (E_{353,\text{HR1}}^b - E_{353,\text{HR2}}^b)_{\text{HM2}}/2$  as

$$\sigma_{V^{EE}}(\text{HL}) = \frac{\sigma_{N^{EE}}}{\sqrt{N_{\text{HL}}}} = 0.02 \mu\text{K}_{\text{CMB}}^2. \quad (37)$$

A similar procedure is applied to compute the uncertainty on  $V^{BB}$ . The ratio of the  $B_{353}$  and  $E_{353}$  variances differs slightly

from the measurement at the power spectra level (Planck Collaboration Int. XXX 2014), probably because of the multipole range over which the ratio of the  $B_{353}$  and  $E_{353}$  variances are computed.

We compute the covariances of the three maps over the high-latitude sky using the relations

$$V^{TE}(\text{HL}) = \frac{1}{N_{\text{HL}}} \sum_{i=1}^{N_{\text{HL}}} D_{353}^b E_{353}^b = (124.1 \pm 1.4) \mu\text{K}_{\text{CMB}}^2, \quad (38)$$

$$V^{TB}(\text{HL}) = \frac{1}{N_{\text{HL}}} \sum_{i=1}^{N_{\text{HL}}} D_{353}^b B_{353}^b = (3.0 \pm 1.5) \mu\text{K}_{\text{CMB}}^2, \quad (39)$$

$$V^{EB}(\text{HL}) = \frac{1}{N_{\text{HL}}} \sum_{i=1}^{N_{\text{HL}}} E_{353}^b B_{353}^b = (-0.2 \pm 0.3) \mu\text{K}_{\text{CMB}}^2. \quad (40)$$

The above covariances divided by  $V^{EE}$  are listed in Table 1. The ratio  $V^{TE}/V^{EE}$  that we find is consistent with the measurements of Planck Collaboration Int. XXX (2014) at the power spectrum level.

## 6.3. Contribution of filaments to the variance of the *E* and *B* maps

In this section, we compute the variance of the  $E_{353}^b$  and  $B_{353}^b$  maps over the sky pixels used to produce the stacked images in Fig. 10, and compare the values with those measured over the HL region. These pixels are within the  $7^\circ \times 5^\circ$  patches, with an orientation angle  $\theta_-$ , centred on the filaments (Sect. 5.1). These pixels define the grey regions in Fig. 12. We label them as SP and the rest of the high-latitude sky as O. The stacking procedure includes the filaments along with their surrounding background emission and, hence, effectively increases the selected fraction of the high-latitude sky,  $f_1$ , from 2.2% (filament pixels as described in Sect. 3.2) to 28%.

We compute the variance from the SP pixels using the relation given in Eq. (34),

$$V^{EE}(\text{SP}) = (137.5 \pm 1.4) \mu\text{K}_{\text{CMB}}^2. \quad (41)$$

The sky variance of the  $E_{353}^b$  map in the high-latitude sky can be written as the sum of contributions from SP ( $f_1 = 0.28$ ) and O ( $1 - f_1 = 0.72$ ) regions. It is given by

$$V^{EE}(\text{HL}) = f_1 \times V^{EE}(\text{SP}) + (1 - f_1) \times V^{EE}(\text{O}). \quad (42)$$

The ratio ( $R_{\text{SP}}$ ) of the variance from the stacked pixels to the total sky variance is given by

$$R_{\text{SP}} = \frac{f_1 \times V^{EE}(\text{SP})}{V^{EE}(\text{HL})} = 0.83. \quad (43)$$

The value of  $R_{\text{SP}}$  is expected to be high, since the filaments are bright structures on the sky. The pixels we used for stacking contribute 83% of the total sky variance in the high-latitude sky. A similar result has been reported for the synchrotron emission, where bright filaments/shells are also measured to contribute most of the sky variance in polarization (Vidal et al. 2015).

It has been noted that the structure in the *Planck* 353 GHz dust polarization maps is not fully accounted for by the filaments seen in the total dust intensity map. In particular, the local dispersion of the polarization angle shows structures in the polarization maps that have no counterpart in total intensity (Planck Collaboration Int. XIX 2015). These structures are thought to trace morphology of  $B_{\text{POS}}$  uncorrelated with matter structures

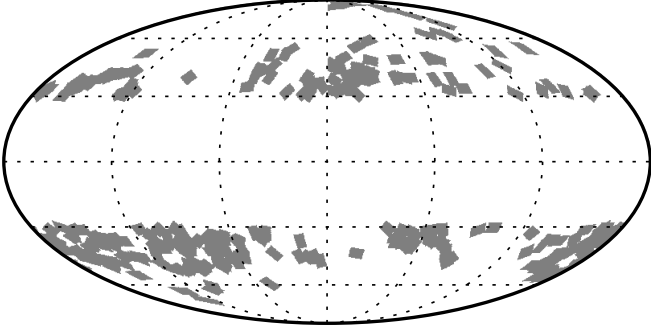


**Fig. 12.** Map of the selected pixels (grey colour) used in the stacking analysis. It covers 28 % of the high-latitude sky. Each tile in the image is a  $7^\circ \times 5^\circ$  patch around the filament centre and rotated by  $\bar{\theta}_-$ .

(Planck Collaboration Int. XX 2015). However, as our  $R_{SP}$  value shows, these polarization structures do not contribute much to the variance of the dust polarization.

In the same way as in Sect. 6.2, we compute the variances  $V^{EE}$ ,  $V^{BB}$ ,  $V^{TE}$ ,  $V^{TB}$ , and  $V^{EB}$  over the SP and O regions. Table 1 presents the ratios of the variances computed over different sky regions.

**Table 1.** The ratios of the variances computed from the selected pixels (SP) used in the stacking analysis and the rest (O) of the high-latitude sky (HL).

Ratio	SP	O	HL
$V^{BB}/V^{EE}$	$0.66 \pm 0.01$	$0.51 \pm 0.05$	$0.62 \pm 0.03$
$V^{TE}/V^{EE}$	$2.74 \pm 0.04$	$2.48 \pm 0.15$	$2.67 \pm 0.07$
$V^{TB}/V^{EE}$	$-0.07 \pm 0.04$	$0.12 \pm 0.04$	$0.06 \pm 0.03$
$V^{EB}/V^{EE}$	$-0.01 \pm 0.02$	$0.02 \pm 0.02$	$0.00 \pm 0.01$

#### 6.4. Analytical approximation

Following Zaldarriaga (2001) and the description of the filaments in Eqs. (19) and (20), we can express the *E*- and *B*-modes of a given filament as

$$\bar{E}_{353}^F \approx -\bar{Q}_{353}^F = \bar{P}_{353}^F \cos 2\Delta_{\bar{\chi}-\bar{\theta}_-}^F, \quad (44)$$

$$\bar{B}_{353}^F \approx -\bar{U}_{353}^F = -\bar{P}_{353}^F \sin 2\Delta_{\bar{\chi}-\bar{\theta}_-}^F, \quad (45)$$

where  $\bar{P}_{353}^F$  is the mean polarization intensity of the filament. The direct relation between  $\bar{E}_{353}^F$  and  $\bar{Q}_{353}^F$ , and  $\bar{B}_{353}^F$  and  $\bar{U}_{353}^F$  only holds for an idealised filament. For  $N$  idealized filaments oriented arbitrarily on the sky with respect to the GN, the ratio between the variances of the *B* and *E* maps is given by

$$\frac{V^{BB}}{V^{EE}} = \frac{\langle \bar{B}_{353}^F \bar{B}_{353}^F \rangle}{\langle \bar{E}_{353}^F \bar{E}_{353}^F \rangle} = \frac{\sum \frac{2\ell+1}{4\pi} C_\ell^{BB} w_\ell^2}{\sum \frac{2\ell+1}{4\pi} C_\ell^{EE} w_\ell^2}, \quad (46)$$

which is expanded in terms of power spectra  $C_\ell^{BB}$  and  $C_\ell^{EE}$  under the assumption of statistical isotropy and homogeneity. The beam window function ( $w_\ell$ ) is the filter function. Both the observed  $C_\ell^{BB}$  and  $C_\ell^{EE}$  dust power spectra follow a power-law

model with the same slope  $\alpha$  (Planck Collaboration Int. XXX 2014). This reduces Eq. (46) to

$$\frac{V^{BB}}{V^{EE}} = \frac{\sum (2\ell+1) A^{BB} \ell^{-\alpha} w_\ell^2}{\sum (2\ell+1) A^{EE} \ell^{-\alpha} w_\ell^2} = \frac{A^{BB}}{A^{EE}}. \quad (47)$$

From the histogram of the upper panel of Fig. 6, the distribution of the angle  $\Delta_{\bar{\chi}-\bar{\theta}_-}^F$  is known for our filament sample. Similar to the assumption made in Sect. 5.2, we assume that all the filaments have the same polarized intensity and therefore

$$\frac{A^{BB}}{A^{EE}} \approx \frac{\langle \sin^2 2\Delta_{\bar{\chi}-\bar{\theta}_-}^F \rangle}{\langle \cos^2 2\Delta_{\bar{\chi}-\bar{\theta}_-}^F \rangle} = 0.66. \quad (48)$$

We have computed the ratio  $A^{BB}/A^{EE}$  using the two independent subsets of the *Planck* data (HM maps) and find the same mean value of 0.66. This value of the  $A^{BB}/A^{EE}$  ratio based on this analytical model matches the observed mean value of  $0.62 \pm 0.03$  (Sect. 6.2). We note that the model value is directly inferred from the distribution of  $\Delta_{\bar{\chi}-\bar{\theta}_-}^F$  for our filament sample. If the HRO of  $\Delta_{\bar{\chi}-\bar{\theta}_-}^F$  was flat with uniform probability between  $-90^\circ$  and  $+90^\circ$ , we would have found equal variances in both the  $E_{353}$  and  $B_{353}$  maps.

In summary, we propose that the alignment between  $\mathbf{B}_{POS}$  and the filament orientations accounts for the *E*-*B* asymmetry in the range of angular scales  $30 < \ell < 300$ . The mean value of  $V^{BB}/V^{EE}$  for O region is consistent with the HL value within  $1.9\sigma$  (Table 1). This shows that a similar alignment between the matter structures and  $\mathbf{B}_{POS}$  can be inferred over the rest of the high-latitude sky. Some high Galactic latitude sky areas, such as the BICEP2 field (BICEP2 Collaboration 2014), do not include any of the strong filaments from our study. The *Planck* 353 GHz polarization maps do not have the required signal-to-noise ratio to measure the  $A^{BB}/A^{EE}$  ratio for individual BICEP2-like fields (Planck Collaboration Int. XXX 2014). Therefore more sensitive observations will be needed to test whether our interpretation is relevant there.

## 7. Relation to Galactic astrophysics

In this section we place the paper results in the context of earlier studies about the filamentary structure of interstellar matter and its correlation with the Galactic magnetic field.

Over the last decades, observations of interstellar gas and dust have been revealing the filamentary structure of the interstellar medium in increasing details. Before *Planck* and *Herschel*, the discovery of the infrared cirrus with the IRAS and Hi all-sky surveys was a main milestone in our perception of the structure of the diffuse ISM (Boulanger 1994; Kalberla & Kerp 2009). At high Galactic latitude, the *Planck* dust emission is tightly correlated with Hi emission at local velocities (Planck Collaboration Int. XVII 2014). In particular, all of the filaments in our sample have an Hi counterpart. They are selected on the 353 GHz map but are seen at far-infrared wavelengths, in particular the IRAS 100  $\mu\text{m}$  map.

The interstellar filaments seen in the *Planck* 353 GHz dust intensity map are not all straight. With our filament-finding algorithm, we have identified the straight segments with lengths  $L \geq 2^\circ$ . Some of these segments are pieces of longer non-straight filaments. The 259 filaments in our sample make most of the sky variance in polarization as measured in our analysis. This is not a complete sample but other filaments at high Galactic latitude do not contribute much to the dust power in *E*-modes.

A number of studies, starting with the pioneering work of Goodman et al. (1990), have used the polarization of background starlight to investigate the relative orientation between the interstellar filaments and  $\mathbf{B}_{\text{POS}}$ . While most studies have targeted filaments identified in extinction maps of molecular clouds in the solar neighbourhood, a few studies have focussed on filaments seen in H $\alpha$  emission (McClure-Griffiths et al. 2006; Clark et al. 2014). These last two papers report a preferred alignment between the filaments and  $\mathbf{B}_{\text{POS}}$  in the diffuse ISM. The analysis of *Planck* data has complemented earlier studies providing greater statistics and sensitivity. Planck Collaboration Int. XXXII (2014) compare the orientations of matter structures identified in the *Planck* 353 GHz map with that of the Galactic magnetic field at intermediate latitudes. The alignment between the filaments and  $\mathbf{B}_{\text{POS}}$  reported in this paper becomes weaker for increasing column density (see Figure 15 of Planck Collaboration Int. XXXII 2014). Towards molecular clouds the relative orientation is observed to change progressively from preferentially parallel in areas with the lowest column density to preferentially perpendicular in the areas with the highest column density (Planck Collaboration Int. XXXV 2015). The transition occurs at a column density of  $10^{21.7} \text{ cm}^{-2}$ . All the filaments considered in our analysis are much below this transition limit and observed, as expected from earlier studies, to be statistically aligned with  $\mathbf{B}_{\text{POS}}$ .

Planck Collaboration Int. XXXII (2014) and Planck Collaboration Int. XXXV (2015) discuss these observational results in light of MHD simulations, which quantify the respective roles of the magnetic field, turbulence, and gas self-gravity in the formation of structures in the magnetized ISM. The alignment between the magnetic field and matter structures in the diffuse ISM is thought to be a signature of turbulence. Simulations show that turbulent flows will tend to stretch gas condensations into sheets and filaments, which appear elongated in column density maps (Hennebelle 2013). These structures will tend to be aligned with the magnetic field where the gas velocity is dynamically aligned with the field (Brandenburg & Lazarian 2013). Alignment also results from the fact that matter and the magnetic field are stretched in the same direction because the field is frozen into matter. The change in relative orientation observed within molecular clouds might be a signature of the formation of gravitationally bound structures in the presence of a dynamically important magnetic field. Indeed, Soler et al. (2013) report a change in the relative orientation between matter structures and the magnetic field, from parallel to perpendicular, for gravitationally bound structures in MHD simulations. This change is most significant for their simulation with the highest magnetization.

## 8. Conclusion

We present a statistical study of the filamentary structure of the 353 GHz *Planck* Stokes maps at high Galactic latitude, relevant to the study of dust emission as a polarization foreground to the CMB. The main results of our work are summarized as follows.

We filter the intensity and polarization maps to isolate structures over the range of angular scales where the *E-B* power asymmetry is observed. From a Hessian analysis of the *Planck* total dust intensity map at 353 GHz, we identify a sample of 259 filaments in the high-latitude sky with lengths  $L \geq 2^\circ$ . We measure the mean orientation angle of each filament in this sample and find that the filaments are statistically aligned with the plane of the sky component of the magnetic field,  $\mathbf{B}_{\text{POS}}$ , inferred from the polarization angles measured by *Planck*. We also find that the orientation of  $\mathbf{B}_{\text{POS}}$  is correlated with that of  $\mathbf{B}_{\text{m,POS}}$  in the solar

neighbourhood. Our results show that the correlation between the structures of interstellar matter and  $\mathbf{B}_{\text{POS}}$  in the diffuse ISM reported in Planck Collaboration Int. XXXII (2014) for intermediate Galactic latitudes also applies to the lower column density filaments (a few  $10^{19} \text{ cm}^{-2}$ ) observed at high Galactic latitude.

We present mean images of our filament sample in dust intensity and Stokes  $Q_{353}$  and  $U_{353}$  with respect to the filament orientation ( $Q'_{353}$  and  $U'_{353}$ ), computed by stacking individual  $7^\circ \times 5^\circ$  patches centred on each filament. The stacked images show that the contribution of the filaments is a negative feature with respect to the background in the  $Q'_{353}$  image and is not seen in the  $U'_{353}$  image. This result directly follows from the fact that the histogram of relative orientation between the filaments and  $\mathbf{B}_{\text{POS}}$  peaks and is symmetric around  $0^\circ$ . Combining the stacked images and the histogram, we estimate the mean polarization fraction of the filaments to be 11 %.

We relate the *E-B* asymmetry discovered in the power spectrum analysis of *Planck* 353 GHz polarization maps (Planck Collaboration Int. XXX 2014) to the alignment between the filaments and  $\mathbf{B}_{\text{POS}}$  in the diffuse ISM. The set of  $7^\circ \times 5^\circ$  patches we stack represents 28 % of the sky area at high Galactic latitude. The power of the *E*-mode dust polarization computed over this area amounts to 83 % of the total dust polarization power in the high-latitude sky. We show with an analytical approximation of the filaments (based on the work of Zaldarriaga 2001), that the HRO between the filaments and  $\mathbf{B}_{\text{POS}}$  may account for the  $C_\ell^{BB}/C_\ell^{EE}$  ratio measured over the high-latitude sky. Our interpretation could also apply to the *E-B* asymmetry reported for the synchrotron emission (Planck Collaboration X 2015), since there is also a correlation between the orientation angle of  $\mathbf{B}_{\text{POS}}$  and the filamentary structures of the synchrotron intensity map (Vidal et al. 2015; Planck Collaboration XXV 2015).

Present models of the dust polarization sky (e.g., O'Dea et al. 2012; Delabrouille et al. 2013) produce an equal amount of power in *E*- and *B*-modes for masks excluding the Galactic plane, because they ignore the correlation between the structure of the magnetic field and that of matter. Our work should motivate a quantitative modelling of the polarized sky, which will take into account the observed correlations between the Galactic magnetic field and the structure of interstellar matter.

*Acknowledgements.* The Planck Collaboration acknowledges the support of: ESA; CNES, and CNRS/INSU-IN2P3-INP (France); ASI, CNR, and INAF (Italy); NASA and DoE (USA); STFC and UKSA (UK); CSIC, MINECO, JA and RES (Spain); Tekes, AoF, and CSC (Finland); DLR and MPG (Germany); CSA (Canada); DTU Space (Denmark); SER/SSO (Switzerland); RCN (Norway); SFI (Ireland); FCT/MCTES (Portugal); ERC and PRACE (EU). A description of the Planck Collaboration and a list of its members, indicating which technical or scientific activities they have been involved in, can be found at <http://www.cosmos.esa.int/web/planck/planck-collaboration>. The research leading to these results has received funding from the European Research Council under the European Union's Seventh Framework Programme (FP7/2007-2013) / ERC grant agreement n° 267934. Some of the results in this paper have been derived using the HEALPix package.

## References

- André, P., Di Francesco, J., Ward-Thompson, D., et al., From Filamentary Networks to Dense Cores in Molecular Clouds: Toward a New Paradigm for Star Formation. 2014, Protostars and Planets VI, 27, [arXiv:1312.6232](https://arxiv.org/abs/1312.6232)
- Arzoumanian, D., André, P., Didelon, P., et al., Characterizing interstellar filaments with Herschel in IC 5146. 2011, A&A, 529, L6, [arXiv:1103.0201](https://arxiv.org/abs/1103.0201)
- BICEP2 Collaboration, Detection of B-Mode Polarization at Degree Angular Scales by BICEP2. 2014, Phys.Rev.Lett., 112, 241101, [arXiv:1403.3985](https://arxiv.org/abs/1403.3985)
- BICEP2/Keck Array and Planck Collaborations, Joint Analysis of BICEP2/Keck Array and Planck Data. 2015, Phys. Rev. Lett., 114, 101301, [arXiv:1502.00612](https://arxiv.org/abs/1502.00612)

- Bond, N. A., Strauss, M. A., & Cen, R., Crawling the cosmic network: exploring the morphology of structure in the galaxy distribution. 2010a, MNRAS, 406, 1609, [arXiv:0903.3601](#)
- Bond, N. A., Strauss, M. A., & Cen, R., Crawling the cosmic network: identifying and quantifying filamentary structure. 2010b, MNRAS, 409, 156, [arXiv:1003.3237](#)
- Boullanger, F. 1994, in *Astronomical Society of the Pacific Conference Series*, Vol. 58, *The First Symposium on the Infrared Cirrus and Diffuse Interstellar Clouds*, ed. R. M. Cutri & W. B. Latter, 101
- Brandenburg, A. & Lazarian, A., *Astrophysical Hydromagnetic Turbulence*. 2013, *Space Sci. Rev.*, 178, 163, [arXiv:1307.5496](#)
- Clark, S. E., Peek, J. E. G., & Putman, M. E., Magnetically Aligned H I Fibers and the Rolling Hough Transform. 2014, *ApJ*, 789, 82, [arXiv:1312.1338](#)
- Colombi, S., Pogosyan, D., & Souradeep, T., Tree Structure of a Percolating Universe. 2000, *Physical Review Letters*, 85, 5515, [arXiv:astro-ph/0011293](#)
- Delabrouille, J., Betoule, M., Melin, J.-B., et al., The pre-launch Planck Sky Model: a model of sky emission at submillimetre to centimetre wavelengths. 2013, A&A, 553, A96, [arXiv:1207.3675](#)
- Forero-Romero, J. E., Hoffman, Y., Gottlöber, S., Klypin, A., & Yepes, G., A dynamical classification of the cosmic web. 2009, MNRAS, 396, 1815, [arXiv:0809.4135](#)
- Goodman, A. A., Bastien, P., Menard, F., & Myers, P. C., Optical polarization maps of star-forming regions in Perseus, Taurus, and Ophiuchus. 1990, *ApJ*, 359, 363
- Górski, K. M., Hivon, E., Banday, A. J., et al., HEALPix: A Framework for High-Resolution Discretization and Fast Analysis of Data Distributed on the Sphere. 2005, *ApJ*, 622, 759, [arXiv:astro-ph/0409513](#)
- Hampel, F. R., The Influence Curve and its Role in Robust Estimation. 1974, *Journal of The American Statistical Association*, 69, 383
- Han, J. L., Manchester, R. N., & Qiao, G. J., Pulsar rotation measures and the magnetic structure of our Galaxy. 1999, MNRAS, 306, 371, [arXiv:astro-ph/9903101](#)
- Heiles, C., The Local Direction and Curvature of the Galactic Magnetic Field Derived from Starlight Polarization. 1996, *ApJ*, 462, 316
- Hennebelle, P., On the origin of non-self-gravitating filaments in the ISM. 2013, A&A, 556, A153, [arXiv:1306.5452](#)
- Kalberla, P. M. W. & Kerp, J., The Hi Distribution of the Milky Way. 2009, *ARA&A*, 47, 27
- Komm, R. W., Gu, Y., Hill, F., Stark, P. B., & Fodor, I. K., Multitaper Spectral Analysis and Wavelet Denoising Applied to Helioseismic Data. 1999, *ApJ*, 519, 407
- Lamarre, J., Puget, J., Ade, P. A. R., et al., *Planck* pre-launch status: The HFI instrument, from specification to actual performance. 2010, A&A, 520, A9
- Lanusse, F., Rassat, A., & Starck, J.-L., Spherical 3D isotropic wavelets. 2012, A&A, 540, A92, [arXiv:1112.0561](#)
- McClure-Griffiths, N. M., Dickey, J. M., Gaensler, B. M., Green, A. J., & Haverkorn, M., Magnetically Dominated Strands of Cold Hydrogen in the Riegel-Crutcher Cloud. 2006, *ApJ*, 652, 1339, [arXiv:astro-ph/0608585](#)
- Men'shchikov, A., A multi-scale filament extraction method: getfilaments. 2013, A&A, 560, A63, [arXiv:1309.2170](#)
- Miville-Deschênes, M.-A., Martin, P. G., Abergel, A., et al., Herschel-SPIRE observations of the Polaris flare: Structure of the diffuse interstellar medium at the sub-parsec scale. 2010, A&A, 518, L104, [arXiv:1005.2746](#)
- Monteserín, C., Barreiro, R. B., Sanz, J. L., & Martínez-González, E., Scalar statistics on the sphere: application to the cosmic microwave background. 2005, MNRAS, 360, 9, [arXiv:astro-ph/0511308](#)
- O'Dea, D. T., Clark, C. N., Contaldi, C. R., & MacTavish, C. J., A model for polarized microwave foreground emission from interstellar dust. 2012, MNRAS, 419, 1795, [arXiv:1107.4612](#)
- Planck Collaboration XI, *Planck* 2013 results. XI. All-sky model of thermal dust emission. 2014, A&A, 571, A11, [arXiv:1312.1300](#)
- Planck Collaboration XIII, *Planck* 2013 results. XIII. Galactic CO emission. 2014, A&A, 571, A13, [arXiv:1303.5073](#)
- Planck Collaboration I, *Planck* 2015 results. I. Overview of products and results. 2015, A&A, submitted, [arXiv:1502.01582](#)
- Planck Collaboration VII, *Planck* 2015 results. VII. High Frequency Instrument data processing: Time-ordered information and beam processing. 2015, A&A, in press, [arXiv:1502.01586](#)
- Planck Collaboration VIII, *Planck* 2015 results. VIII. High Frequency Instrument data processing: Calibration and maps. 2015, A&A, submitted, [arXiv:1502.01587](#)
- Planck Collaboration X, *Planck* 2015 results. X. Diffuse component separation: Foreground maps. 2015, A&A, submitted, [arXiv:1502.01588](#)
- Planck Collaboration XXV, *Planck* 2015 results. XXV. Diffuse, low-frequency Galactic foregrounds. 2015, A&A, submitted, [arXiv:1506.06660](#)
- Planck Collaboration Int. XVII, *Planck* intermediate results. XVII. Emission of dust in the diffuse interstellar medium from the far-infrared to microwave frequencies. 2014, A&A, 566, A55, [arXiv:1312.5446](#)
- Planck Collaboration Int. XIX, *Planck* intermediate results. XIX. An overview of the polarized thermal emission from Galactic dust. 2015, A&A, 576, A104, [arXiv:1405.0871](#)
- Planck Collaboration Int. XX, *Planck* intermediate results. XX. Comparison of polarized thermal emission from Galactic dust with simulations of MHD turbulence. 2015, A&A, 576, A105, [arXiv:1405.0872](#)
- Planck Collaboration Int. XXI, *Planck* intermediate results. XXI. Comparison of polarized thermal emission from Galactic dust at 353 GHz with optical interstellar polarization. 2015, A&A, 576, A106, [arXiv:1405.0873](#)
- Planck Collaboration Int. XXII, *Planck* intermediate results. XXII. Frequency dependence of thermal emission from Galactic dust in intensity and polarization. 2015, A&A, 576, A107, [arXiv:1405.0874](#)
- Planck Collaboration Int. XXX, *Planck* intermediate results. XXX. The angular power spectrum of polarized dust emission at intermediate and high Galactic latitudes. 2014, A&A, in press, [arXiv:1409.5738](#)
- Planck Collaboration Int. XXXII, *Planck* intermediate results. XXXII. The relative orientation between the magnetic field and structures traced by interstellar dust. 2014, A&A, in press, [arXiv:1409.6728](#)
- Planck Collaboration Int. XXXIII, *Planck* intermediate results. XXXIII. Signature of the magnetic field geometry of interstellar filaments in dust polarization maps. 2014, A&A, in press, [arXiv:1411.2271](#)
- Planck Collaboration Int. XXXV, *Planck* intermediate results. XXXV. Probing the role of the magnetic field in the formation of structure in molecular clouds. 2015, A&A, in press, [arXiv:1502.04123](#)
- Polychroni, D., Schisano, E., Elia, D., et al., Two Mass Distributions in the L 1641 Molecular Clouds: The Herschel Connection of Dense Cores and Filaments in Orion A. 2013, *ApJ*, 777, L33, [arXiv:1309.2332](#)
- Rand, R. J. & Lyne, A. G., New Rotation Measures of Distant Pulsars in the Inner Galaxy and Magnetic Field Reversals. 1994, MNRAS, 268, 497
- Soler, J. D., Hennebelle, P., Martin, P. G., et al., An Imprint of Molecular Cloud Magnetization in the Morphology of the Dust Polarized Emission. 2013, *ApJ*, 774, 128, [arXiv:1303.1830](#)
- Sousbie, T., The persistent cosmic web and its filamentary structure - I. Theory and implementation. 2011, MNRAS, 414, 350, [arXiv:1009.4015](#)
- Starck, J.-L., Moudou, Y., Abrial, P., & Nguyen, M., Wavelets, ridgelets and curvelets on the sphere. 2006, A&A, 446, 1191, [arXiv:astro-ph/0509883](#)
- Vidal, M., Dickinson, C., Davies, R. D., & Leahy, J. P., Polarized radio filaments outside the Galactic plane. 2015, MNRAS, 452, 656, [arXiv:1410.4438](#)
- Zaldarriaga, M., Nature of the E-B decomposition of CMB polarization. 2001, *Phys. Rev. D*, 64, 103001, [arXiv:astro-ph/0106174](#)

## Appendix A: Hessian analysis

In this appendix, we detail the implementation of the Hessian analysis to determine the orientations of the filaments. We start with the  $D_{353}^b$  map at HEALPix resolution  $N_{\text{side}} = 512$ . For each pixel on the sky, we estimate the first and second derivatives of  $D_{353}^b$  with respect to the Galactic longitude  $l$  and latitude  $b$  (as described in [Monteserín et al. 2005](#)). The Hessian matrix of  $D_{353}^b$  is defined as

$$H = \begin{bmatrix} H_{xx} & H_{xy} \\ H_{xy} & H_{yy} \end{bmatrix}, \quad (\text{A.1})$$

where

$$H_{xx} = \frac{\partial^2 D_{353}^b}{\partial b^2}, \quad (\text{A.2})$$

$$H_{xy} = \frac{\partial^2 D_{353}^b}{\cos b \partial b \partial l}, \quad (\text{A.3})$$

$$H_{yy} = \frac{\partial^2 D_{353}^b}{\cos^2 b \partial l^2}. \quad (\text{A.4})$$

We decompose the  $D_{353}^b$  map into  $a_{\ell m}$  coefficients using the “ianafast” routine of HEALPix and then use the “isynfast” routine in HEALPix to compute the second partial derivatives at each pixel. This method is computationally faster than the one used in [Planck Collaboration Int. XXXII \(2014\)](#). The smallest eigenvalue,  $\lambda_-$ , of the Hessian matrix is calculated as

$$\lambda_- = \frac{1}{2}(H_{xx} + H_{yy} - \alpha), \quad (\text{A.5})$$

where  $\alpha = \sqrt{(H_{xx} - H_{yy})^2 + 4H_{xy}^2}$ . The map of  $\lambda_-$ , displayed in the lower left panel of Fig. 2, highlights the filaments in the  $D_{353}^b$  map. The filament orientation angle,  $\theta_-$ , is calculated using the relation

$$\theta_- = \text{atan} \left[ -\frac{H_{xx} - H_{yy} + \alpha}{2H_{xy}} \right]. \quad (\text{A.6})$$

This follows the IAU convention, since it is measured from the GN and positive to the East direction. The formula for the filament orientation angle  $\theta_-$  is equivalent to equation (9) of Planck Collaboration Int. XXXII (2014).

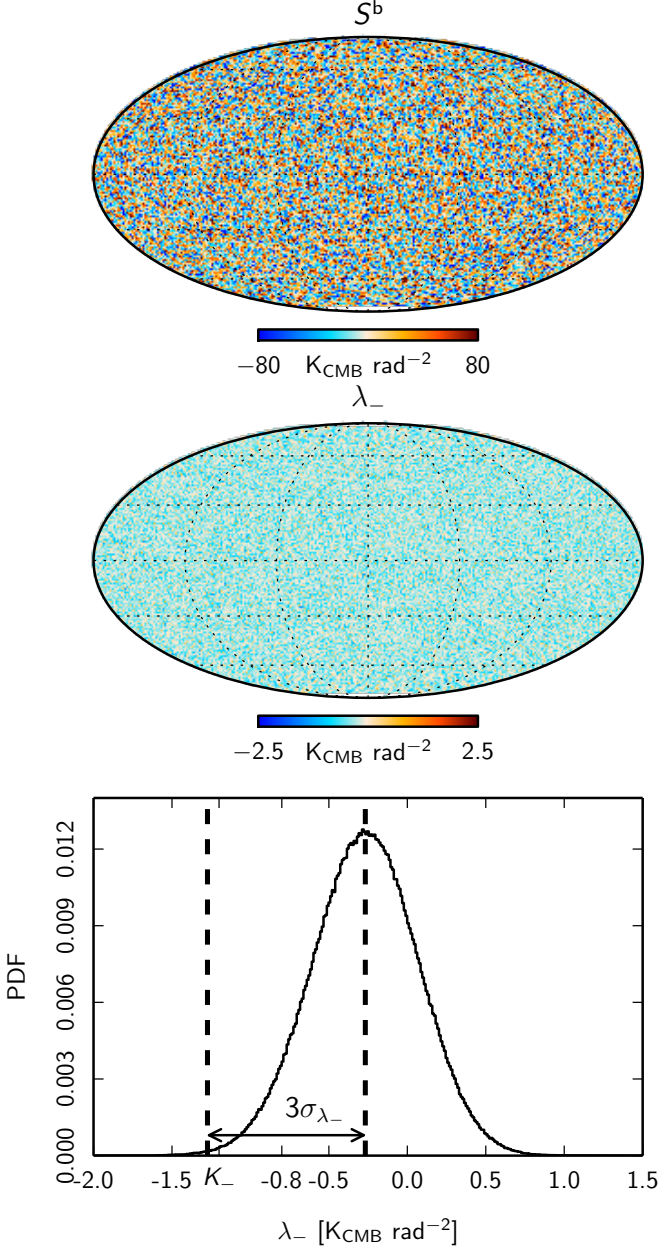


**Fig. A.1.** Filtered realization of the Gaussian dust sky (upper panel) and the corresponding eigenvalue  $\lambda_-$  (middle panel). The distribution of the eigenvalue  $\lambda_-$  (lower panel) over the unmasked pixels is Gaussian.

## Appendix B: Gaussian realization of the dust sky

Here we apply the SMAFF algorithm on a Gaussian realization of the dust total intensity map using the same methodology as described in Sect. 3.2. The power spectrum is modelled as  $C_\ell^{TT} \propto \ell^\alpha$ , where  $\alpha$  is the slope of the power law. We choose  $\alpha = -2.4$  in the multipole range from  $\ell = 30$  to 300 (Planck Collaboration Int. XXII 2015).

We compute a Gaussian realization of a sky map on a HEALPix grid with an  $\ell^{-2.4}$  power spectrum, and use the spline wavelet transform to filter it. Hereafter, we refer to the filtered simulated Gaussian map as the “ $S^b$  map”. We compute the smallest eigenvalue  $\lambda_-$  of the  $S^b$  map using the Hessian analysis described in Appendix A. The  $S^b$  map and its corresponding  $\lambda_-$  map are shown in the upper and middle panels of Fig. A.1.

We only consider the high-latitude sky. With the upper threshold  $K_- = m_{\lambda_-} - 3\sigma_{\lambda_-}$ , we remove pixels as shown in the lower panel of Fig. A.1. Running our friend-of-friend algorithm on the  $S^b$  map, we do not detect any filament with  $L \geq 2^\circ$ . For higher values of the threshold  $K_-$ , we detect such filaments in the  $S^b$  map. We call them “weak” filaments. The threshold factor  $K_-$ , used in our study, is a key factor to separate the strong filaments from the weak ones. The main results of this paper follow from the statistical properties of strong filaments. However, in Appendix C we demonstrate that they still hold for the weak filaments.

## Appendix C: Effect of $\lambda_-$ thresholding on the filament count

We apply the threshold  $K_- = m_{\lambda_-} - 3\sigma_{\lambda_-}$  in Sect. 3.2 to find strong filaments in the  $D_{353}^b$  map. In this section, we change the threshold  $K_-$  to quantify its effect on the HRO between the filaments and  $B_{\text{POS}}$ . We choose different thresholds and divide the selected  $\lambda_-$  coherent structures into two categories, namely strong and weak filaments. The strong filaments are selected from the sky pixels that have  $\lambda_- < m_{\lambda_-} - 3\sigma_{\lambda_-}$ . Whereas, the weak filaments are selected from the sky pixels that have  $m_{\lambda_-} - 3\sigma_{\lambda_-} \leq \lambda_- < m_{\lambda_-} - p\sigma_{\lambda_-}$ , where  $p$  is a factor to defined the threshold  $K_- = m_{\lambda_-} - p\sigma_{\lambda_-}$ . In Table C.1, we list the number of weak filaments for different values of  $p$ .

By choosing a threshold  $K_- = m_{\lambda_-} - 1\sigma_{\lambda_-}$  and running our friend-of-friend algorithm on the  $D_{353}^b$  map, we double the number of filaments with  $L \geq 2^\circ$ . For this larger set, we compute the HRO between the filaments and  $B_{\text{POS}}$ , and present it in Fig. C.1. The  $1\sigma$  dispersion of the angle difference remains the same as for our nominal set. This shows that the alignment between the structures of interstellar matter and  $B_{\text{POS}}$  holds even when including the weak filaments.

Including the weak filaments and their surrounding background emission in the analysis of Sect. 6.3 effectively increases the sky fraction from 28% to 50% of the high-latitude sky. With more sky coverage, the ratio of the variances, i.e.,  $V^{BB}/V^{EE}$ ,  $V^{TE}/V^{EE}$ ,  $V^{TB}/V^{EE}$ , and  $V^{EB}/V^{EE}$  is close to the HL region values quoted in Table 1.

## Appendix D: Uncertainties on the angles $\bar{\theta}_-$ and $\bar{\chi}$

In Sect. 4 we present our statistical analysis of the relative orientation between the filaments and  $B_{\text{POS}}$ . The filament orientation angle,  $\theta_-$ , is a single number computed from the  $D_{353}^b$  map. To estimate the error bar on  $\bar{\theta}_-$ , we propagate the noise in the  $D_{353}$  map ( $N_{D_{353}}$ ) through the Hessian analysis. We simulate a

**Table C.1.** Total filament count, including the strong and weak filaments, as a function of the threshold  $K_-$  on the  $\lambda_-$  map derived from the  $D_{353}^b$  map.

Factor $p$	Filament count			total
	weak $m_{\lambda_-} - 3\sigma_{\lambda_-} \leq \lambda_- < m_{\lambda_-} - p\sigma_{\lambda_-}$	strong $\lambda_- < m_{\lambda_-} - 3\sigma_{\lambda_-}$		
3	0	259		259
2	53	259		312
1.5	140	259		399
1	259	259		518

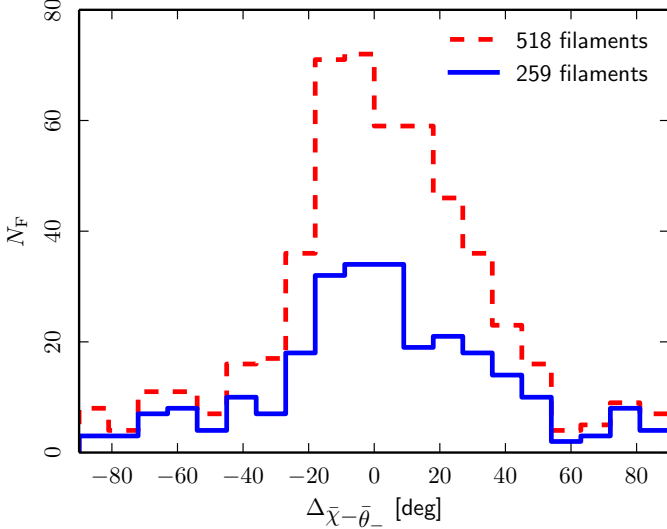


**Fig. C.1.** Same as the upper panel of Fig. 6, when including angle differences  $\Delta\bar{\chi}-\bar{\theta}_-$  from the weak filaments. The width of the histogram does not change.

Gaussian realization of the  $N_{D_{353}}$  map and add it to the  $D_{353}$  map. We filter the noise added to the  $D_{353}$  map in the same manner as the  $D_{353}$  map. For each filament in our sample, we compute the change of its orientation angle from the added noise using the formula

$$\Delta\bar{\theta}_- = \bar{\theta}_-(D_{353}^b + N_{D_{353}}^b) - \bar{\theta}_-(D_{353}^b). \quad (\text{D.1})$$

The distribution of the angle difference is presented with red colour in Fig. D.1. The mean of the distribution is  $0^\circ$  and the  $1\sigma$  dispersion is  $0.2^\circ$ . This shows that the noise in the  $D_{353}$  map has little impact on our estimate of the filament orientation angle.

Next, we compute the uncertainty on the orientation angle of  $\mathbf{B}_{\text{POS}}$ . We use the two HM *Planck* polarization maps, and compute the orientation angle of  $\mathbf{B}_{\text{POS}}$  using Eq. (2). For each filament in our sample, we compute the difference between the two values obtained from the two HM maps,

$$\Delta\bar{\chi} = 0.5 \times [\bar{\chi}_{\text{HM1}} - \bar{\chi}_{\text{HM2}}]. \quad (\text{D.2})$$

The histogram of the angle difference is presented with blue colour in Fig. D.1. The mean of the distribution is  $0^\circ$  and the  $1\sigma$  dispersion is  $2^\circ$ . The error on the orientation angle of  $\mathbf{B}_{\text{POS}}$  is small compared to the width of the HROs in Fig. 6.

Last, we assess the impact of the map filtering on our analysis, computing the mean orientations of the filaments, over the same set of selected pixels, on the  $D_{353}$  map. We compute the

angle difference of the filament orientation derived from the filtered and unfiltered *Planck* 353 GHz maps

$$\Delta\Theta = \bar{\theta}_-(D_{353}) - \bar{\theta}_-(D_{353}^b). \quad (\text{D.3})$$

The histogram of  $\Delta\Theta$  is plotted with green colour in Fig. D.1. The mean of the distribution is  $0^\circ$  and the  $1\sigma$  dispersion is  $7.0^\circ$ . All the uncertainties measured in  $\bar{\theta}_-$  and  $\bar{\chi}$  are small compared to the dispersion of the HRO measured in Fig. 6. This means that the data noise (for the intensity and polarization maps) and the filtering of the data are not critical for our study.

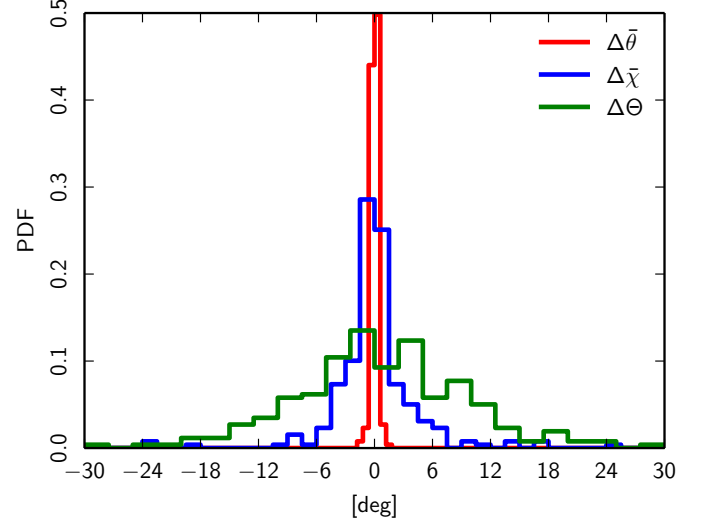


**Fig. D.1.** Histogram of changes in  $\bar{\theta}_-$  (red) and  $\bar{\chi}$  (blue) due to noise present in the *Planck* data. The histogram of changes in  $\bar{\theta}_-$  from the difference of the filtered and unfiltered  $D_{353}$  maps is shown in green.

- <sup>1</sup> APC, AstroParticule et Cosmologie, Université Paris Diderot, CNRS/IN2P3, CEA/Irfu, Observatoire de Paris, Sorbonne Paris Cité, 10, rue Alice Domon et Léonie Duquet, 75205 Paris Cedex 13, France
- <sup>2</sup> Aalto University Metsähovi Radio Observatory, P.O. Box 13000, FI-00076 AALTO, Finland
- <sup>3</sup> African Institute for Mathematical Sciences, 6-8 Melrose Road, Muizenberg, Cape Town, South Africa
- <sup>4</sup> Agenzia Spaziale Italiana Science Data Center, Via del Politecnico snc, 00133, Roma, Italy
- <sup>5</sup> Astrophysics Group, Cavendish Laboratory, University of Cambridge, J J Thomson Avenue, Cambridge CB3 0HE, U.K.
- <sup>6</sup> Astrophysics & Cosmology Research Unit, School of Mathematics, Statistics & Computer Science, University of KwaZulu-Natal, Westville Campus, Private Bag X54001, Durban 4000, South Africa
- <sup>7</sup> Atacama Large Millimeter/submillimeter Array, ALMA Santiago Central Offices, Alonso de Cordova 3107, Vitacura, Casilla 763 0355, Santiago, Chile
- <sup>8</sup> CITA, University of Toronto, 60 St. George St., Toronto, ON M5S 3H8, Canada
- <sup>9</sup> CNRS, IRAP, 9 Av. colonel Roche, BP 44346, F-31028 Toulouse cedex 4, France
- <sup>10</sup> California Institute of Technology, Pasadena, California, U.S.A.
- <sup>11</sup> Centro de Estudios de Física del Cosmos de Aragón (CEFCA), Plaza San Juan, 1, planta 2, E-44001, Teruel, Spain
- <sup>12</sup> Computational Cosmology Center, Lawrence Berkeley National Laboratory, Berkeley, California, U.S.A.
- <sup>13</sup> Consejo Superior de Investigaciones Científicas (CSIC), Madrid, Spain



- <sup>14</sup> DSM/Irfu/SPP, CEA-Saclay, F-91191 Gif-sur-Yvette Cedex, France
- <sup>15</sup> DTU Space, National Space Institute, Technical University of Denmark, Elektrovej 327, DK-2800 Kgs. Lyngby, Denmark
- <sup>16</sup> Département de Physique Théorique, Université de Genève, 24, Quai E. Ansermet, 1211 Genève 4, Switzerland
- <sup>17</sup> Departamento de Astrofísica, Universidad de La Laguna (ULL), E-38206 La Laguna, Tenerife, Spain
- <sup>18</sup> Departamento de Física, Universidad de Oviedo, Avda. Calvo Sotelo s/n, Oviedo, Spain
- <sup>19</sup> Department of Astrophysics/IMAPP, Radboud University Nijmegen, P.O. Box 9010, 6500 GL Nijmegen, The Netherlands
- <sup>20</sup> Department of Physics & Astronomy, University of British Columbia, 6224 Agricultural Road, Vancouver, British Columbia, Canada
- <sup>21</sup> Department of Physics and Astronomy, Dana and David Dornsife College of Letter, Arts and Sciences, University of Southern California, Los Angeles, CA 90089, U.S.A.
- <sup>22</sup> Department of Physics and Astronomy, University College London, London WC1E 6BT, U.K.
- <sup>23</sup> Department of Physics, Florida State University, Keen Physics Building, 77 Chieftan Way, Tallahassee, Florida, U.S.A.
- <sup>24</sup> Department of Physics, Gustaf Hällströmin katu 2a, University of Helsinki, Helsinki, Finland
- <sup>25</sup> Department of Physics, Princeton University, Princeton, New Jersey, U.S.A.
- <sup>26</sup> Department of Physics, University of California, Santa Barbara, California, U.S.A.
- <sup>27</sup> Department of Physics, University of Illinois at Urbana-Champaign, 1110 West Green Street, Urbana, Illinois, U.S.A.
- <sup>28</sup> Dipartimento di Fisica e Astronomia G. Galilei, Università degli Studi di Padova, via Marzolo 8, 35131 Padova, Italy
- <sup>29</sup> Dipartimento di Fisica e Scienze della Terra, Università di Ferrara, Via Saragat 1, 44122 Ferrara, Italy
- <sup>30</sup> Dipartimento di Fisica, Università La Sapienza, P. le A. Moro 2, Roma, Italy
- <sup>31</sup> Dipartimento di Fisica, Università degli Studi di Milano, Via Celoria, 16, Milano, Italy
- <sup>32</sup> Dipartimento di Matematica, Università di Roma Tor Vergata, Via della Ricerca Scientifica, 1, Roma, Italy
- <sup>33</sup> Discovery Center, Niels Bohr Institute, Blegdamsvej 17, Copenhagen, Denmark
- <sup>34</sup> European Southern Observatory, ESO Vitacura, Alonso de Cordova 3107, Vitacura, Casilla 19001, Santiago, Chile
- <sup>35</sup> European Space Agency, ESAC, Planck Science Office, Camino bajo del Castillo, s/n, Urbanización Villafranca del Castillo, Villanueva de la Cañada, Madrid, Spain
- <sup>36</sup> European Space Agency, ESTEC, Keplerlaan 1, 2201 AZ Noordwijk, The Netherlands
- <sup>37</sup> Facoltà di Ingegneria, Università degli Studi e-Campus, Via Isimbardi 10, Novedrate (CO), 22060, Italy
- <sup>38</sup> Finnish Centre for Astronomy with ESO (FINCA), University of Turku, Väisäläntie 20, FIN-21500, Piikkiö, Finland
- <sup>39</sup> Gran Sasso Science Institute, INFN, viale F. Crispi 7, 67100 L'Aquila, Italy
- <sup>40</sup> HGSFP and University of Heidelberg, Theoretical Physics Department, Philosophenweg 16, 69120, Heidelberg, Germany
- <sup>41</sup> Helsinki Institute of Physics, Gustaf Hällströmin katu 2, University of Helsinki, Helsinki, Finland
- <sup>42</sup> INAF - Osservatorio Astrofisico di Catania, Via S. Sofia 78, Catania, Italy
- <sup>43</sup> INAF - Osservatorio Astronomico di Padova, Vicolo dell'Osservatorio 5, Padova, Italy
- <sup>44</sup> INAF - Osservatorio Astronomico di Roma, via di Frascati 33, Monte Porzio Catone, Italy
- <sup>45</sup> INAF - Osservatorio Astronomico di Trieste, Via G.B. Tiepolo 11, Trieste, Italy
- <sup>46</sup> INAF/IASF Bologna, Via Gobetti 101, Bologna, Italy
- <sup>47</sup> INAF/IASF Milano, Via E. Bassini 15, Milano, Italy
- <sup>48</sup> INFN, Sezione di Bologna, Via Irnerio 46, I-40126, Bologna, Italy
- <sup>49</sup> INFN, Sezione di Roma 1, Università di Roma Sapienza, Piazzale Aldo Moro 2, 00185, Roma, Italy
- <sup>50</sup> INFN, Sezione di Roma 2, Università di Roma Tor Vergata, Via della Ricerca Scientifica, 1, Roma, Italy
- <sup>51</sup> IPAG: Institut de Planétologie et d'Astrophysique de Grenoble, Université Grenoble Alpes, IPAG, F-38000 Grenoble, France, CNRS, IPAG, F-38000 Grenoble, France
- <sup>52</sup> Imperial College London, Astrophysics group, Blackett Laboratory, Prince Consort Road, London, SW7 2AZ, U.K.
- <sup>53</sup> Infrared Processing and Analysis Center, California Institute of Technology, Pasadena, CA 91125, U.S.A.
- <sup>54</sup> Institut Universitaire de France, 103, bd Saint-Michel, 75005, Paris, France
- <sup>55</sup> Institut d'Astrophysique Spatiale, CNRS (UMR8617) Université Paris-Sud 11, Bâtiment 121, Orsay, France
- <sup>56</sup> Institut d'Astrophysique de Paris, CNRS (UMR7095), 98 bis Boulevard Arago, F-75014, Paris, France
- <sup>57</sup> Institute of Astronomy, University of Cambridge, Madingley Road, Cambridge CB3 0HA, U.K.
- <sup>58</sup> Institute of Theoretical Astrophysics, University of Oslo, Blindern, Oslo, Norway
- <sup>59</sup> Instituto Nacional de Astrofísica, Óptica y Electrónica (INAOE), Apartado Postal 51 y 216, 72000 Puebla, México
- <sup>60</sup> Instituto de Astrofísica de Canarias, C/Vía Láctea s/n, La Laguna, Tenerife, Spain
- <sup>61</sup> Instituto de Física de Cantabria (CSIC-Universidad de Cantabria), Avda. de los Castros s/n, Santander, Spain
- <sup>62</sup> Istituto Nazionale di Fisica Nucleare, Sezione di Padova, via Marzolo 8, I-35131 Padova, Italy
- <sup>63</sup> Jet Propulsion Laboratory, California Institute of Technology, 4800 Oak Grove Drive, Pasadena, California, U.S.A.
- <sup>64</sup> Jodrell Bank Centre for Astrophysics, Alan Turing Building, School of Physics and Astronomy, The University of Manchester, Oxford Road, Manchester, M13 9PL, U.K.
- <sup>65</sup> Kavli Institute for Cosmological Physics, University of Chicago, Chicago, IL 60637, USA
- <sup>66</sup> Kavli Institute for Cosmology Cambridge, Madingley Road, Cambridge, CB3 0HA, U.K.
- <sup>67</sup> LAL, Université Paris-Sud, CNRS/IN2P3, Orsay, France
- <sup>68</sup> LERMA, CNRS, Observatoire de Paris, 61 Avenue de l'Observatoire, Paris, France
- <sup>69</sup> Laboratoire AIM, IRFU/Service d'Astrophysique - CEA/DSM - CNRS - Université Paris Diderot, Bât. 709, CEA-Saclay, F-91191 Gif-sur-Yvette Cedex, France
- <sup>70</sup> Laboratoire Traitement et Communication de l'Information, CNRS (UMR 5141) and Télécom ParisTech, 46 rue Barrault F-75634 Paris Cedex 13, France
- <sup>71</sup> Laboratoire de Physique Subatomique et Cosmologie, Université Grenoble-Alpes, CNRS/IN2P3, 53, rue des Martyrs, 38026 Grenoble Cedex, France
- <sup>72</sup> Laboratoire de Physique Théorique, Université Paris-Sud 11 & CNRS, Bâtiment 210, 91405 Orsay, France
- <sup>73</sup> Lawrence Berkeley National Laboratory, Berkeley, California, U.S.A.
- <sup>74</sup> Lebedev Physical Institute of the Russian Academy of Sciences, Astro Space Centre, 84/32 Profsoyuznaya st., Moscow, GSP-7, 117997, Russia
- <sup>75</sup> Max-Planck-Institut für Astrophysik, Karl-Schwarzschild-Str. 1, 85741 Garching, Germany
- <sup>76</sup> National University of Ireland, Department of Experimental Physics, Maynooth, Co. Kildare, Ireland
- <sup>77</sup> Nicolaus Copernicus Astronomical Center, Bartycka 18, 00-716 Warsaw, Poland
- <sup>78</sup> Niels Bohr Institute, Blegdamsvej 17, Copenhagen, Denmark
- <sup>79</sup> Optical Science Laboratory, University College London, Gower Street, London, U.K.
- <sup>80</sup> SISSA, Astrophysics Sector, via Bonomea 265, 34136, Trieste, Italy

- <sup>81</sup> School of Physics and Astronomy, Cardiff University, Queens Buildings, The Parade, Cardiff, CF24 3AA, U.K.
- <sup>82</sup> Simon Fraser University, Department of Physics, 8888 University Drive, Burnaby BC, Canada
- <sup>83</sup> Sorbonne Université-UPMC, UMR7095, Institut d'Astrophysique de Paris, 98 bis Boulevard Arago, F-75014, Paris, France
- <sup>84</sup> Space Research Institute (IKI), Russian Academy of Sciences, Profsoyuznaya Str, 84/32, Moscow, 117997, Russia
- <sup>85</sup> Space Sciences Laboratory, University of California, Berkeley, California, U.S.A.
- <sup>86</sup> Special Astrophysical Observatory, Russian Academy of Sciences, Nizhnij Arkhyz, Zelenchukskiy region, Karachai-Cherkessian Republic, 369167, Russia
- <sup>87</sup> Sub-Department of Astrophysics, University of Oxford, Keble Road, Oxford OX1 3RH, U.K.
- <sup>88</sup> UPMC Univ Paris 06, UMR7095, 98 bis Boulevard Arago, F-75014, Paris, France
- <sup>89</sup> Université de Toulouse, UPS-OMP, IRAP, F-31028 Toulouse cedex 4, France
- <sup>90</sup> Universities Space Research Association, Stratospheric Observatory for Infrared Astronomy, MS 232-11, Moffett Field, CA 94035, U.S.A.
- <sup>91</sup> University of Granada, Departamento de Física Teórica y del Cosmos, Facultad de Ciencias, Granada, Spain
- <sup>92</sup> University of Granada, Instituto Carlos I de Física Teórica y Computacional, Granada, Spain
- <sup>93</sup> Warsaw University Observatory, Aleje Ujazdowskie 4, 00-478 Warszawa, Poland